X-RAY SPECTROMETRY
*X-Ray Spectrom.* **29**, 73–91 (2000)

# Use of Microscopic XRF for Non-destructive Analysis in Art and Archaeometry

**K. Janssens,[1]* G. Vittiglio,[1] I. Deraedt,[1] A. Aerts,[1] B. Vekemans,[1] L. Vincze,[1] F. Wei,[1] I. Deryck,[1] O. Schalm,[1] F. Adams,[1] A. Rindby,[2] A. Knöchel,[3] A. Simionovici[4] and A. Snigirev[4]**

[1] Department of Chemistry, University of Antwerp (UIA), Antwerp, Belgium
[2] Department of Physics, Chalmers University of Technology, Göteborg, Sweden
[3] Institut für Angewandte und Anorganische Chemie, Universität Hamburg, Hamburg, Germany
[4] Experimental Division, European Synchrotron Radiation Facility, Grenoble, France

**The various application possibilities of microscopic x-ray fluorescence and associated methods for the characterization and provenance analysis of objects and materials of cultural heritage value are discussed by means of a number of case studies. They include the trace analysis of historic glass, the analysis of corroded coins and statues in bronze and silver and the study of inks on historical documents. These studies are conducted by means of micro-XRF instruments installed at synchrotron beamlines and by means of laboratory equipment, some of which is easily transportable to the museum or archaeological site where the objects of interest are located.** **Copyright © 2000 John Wiley & Sons, Ltd.**

## INTRODUCTION

Modern studies on objects and materials of historical and/or cultural value usually involve the use of various analytical methods and techniques to extract objective information from these materials; in many cases, the chemical composition (major elements to traces) is the primary type of information that is needed. The objects involved are often unique in nature (e.g. paintings, statues, utilitarian objects of different shapes and sizes in metal, glass, wood, stone, ceramics, etc.). They can be in unadorned state or covered with multi-coloured decorations, and may be well preserved or in a serious state of decline.

Studies involving scientific methods may be undertaken with the aim of elucidating the provenance of the object under study. Usually such studies seek to increase the knowledge on the historical context, e.g. the determination of the composition of bronze-age artifacts from different periods and geographical locations may help to elucidate the early evolution of metallurgical technology and its geographical spread.[1] Next to this cultural–historical perspective, scientific methods may also be employed to assess the state of conservation of a particular material; the information obtained may be used to select the most appropriate means of conservation or restoration. Similarly, objects that have been subjected to a restoration treatment (in the recent or not so recent past) may be investigated to distinguish original from add-on materials or to evaluate the effectiveness of past treatments. Finally, scientific methods are also used to allow (more) objective authentication of (usually valuable) art and cultural objects.

* Correspondence to: K. Janssens, Departement Scheikunde, Universiteit Antwerpen Universiteitsplein l, B-2610 Antwerp, Belgium.

According to Lahanier *et al.*,[2] an ideal method for analyzing objects of artistic, historic or archaeological nature should be:

(a) *non-destructive*, i.e. respecting the physical integrity of the material/object. Often valuable objects can only be investigated when the analysis does not result in any (visible) damage; usually this completely eliminates sampling or limits it to very small amounts;
(b) *fast*, so that large numbers of similar objects may be analysed or a single object investigated at various positions on its surface; this property is very valuable since this is the only way of being able to discern between general trends in the data and outlying objects or data points;
(c) *universal*, so that by means of a single instrument, many materials and objects of various shapes and dimensions may be analysed with minimal sample pretreatment;
(d) *versatile*, allowing with the same technique average compositional information to be obtained, but also local information of small areas (e.g. millimetre to micrometre-sized) from heterogeneous materials;
(e) *sensitive*, so that object grouping and other types of provenance analysis can be done not only by means of major elements but also by means of trace-element fingerprints; and
(f) *multi-elemental*, so that in a single measurement, information on many elements is obtained simultaneously and, more importantly, so that also information is obtained on elements which were not initially thought to be relevant to the investigation.

A number of examples of the use of (micro)analytical techniques suitable for characterizing archaeological and artistic materials were recently described by Adams *et al.*[3] An extensive overview of the use of proton micro beams for analysing a variety of artistic/archaeological materials such as (gem)stones, pottery, glass, metallic objects,

CCC 0049–8246/2000/010073–19 $17.50
Copyright © 2000 John Wiley & Sons, Ltd.
*Received 19 July 1999*
*Accepted 20 October 1999*

calcified tissues, paper and pigments by means of proton-induced x-ray emission (PIXE) and related techniques is provided by Malmqvist.[4]

Since XRF meets a number of the above requirements, analysis of objects of artistic and/or archaeological value with conventional XRF is fairly common; it is in fact one of the most often applied methods for obtaining qualitative and semi-quantitative information on the materials of which these objects are made.[5,6] On the other hand, the use of conventional XRF for reliable quantitative analysis is severely hampered by the fact that the irradiated area is usually large. This prevents the separate analysis of details of decorations, distinct features, etc. Also, the irradiation geometry and sample surface are usually non-ideal and/or not well defined, possibly introducing systematic errors in the quantification. The use of smaller x-ray beams can circumvent some of these limitations. In such as case, motorized sample movement allows the local analysis capability to be extended towards two-dimensional imaging of certain elements on the surface of artifacts. Since many objects of artistic and/or archaeological nature are fairly large and bulky (e.g. statues, oil paintings, vases, treasury objects), instrumentation that can accommodate objects of various shapes and is able to operate in air atmosphere is very useful. Usually, this implies that the equipment is laboratory-built as, for reasons of radiation protection, commercially available instruments mostly are equipped with relatively small, well-shielded sample compartments.

Depending on the nature of the investigation and on the type of information required, one of the various forms of $\mu$-XRF may be employed.

Synchrotron ($\mu$-)XRF, offering ppm level detectability for many elements,[7] can be used for quantitative fingerprint analysis of materials in order to gain a better understanding of their provenance. The use of a microscopic beam permits the detailed investigation of the processes that have altered the surface composition of the material. Although suitable for trace-level microanalysis of organic materials (e.g. paper, pigments dispersed in a organic binder) or for silicate-rich materials such as pottery or glass, the high primary intensity of synchrotron microbeams is usually not compatible with the analysis of metallic materials (e.g. artifacts made of bronze, iron, silver, gold or alloys of these metals).

However, laboratory $\mu$-XRF can be conveniently used for this purpose. Another strong point of laboratory $\mu$-XRF is the possibility of performing local (quantitative) analysis on objects whose size, shape or nature is incompatible with the vacuum and the small sample enclosures employed by most conventional microanalytical techniques such as EPXMA and $\mu$-PIXE. In this respect, $\mu$-XRF offers similar possibilities to external-beam PIXE,[6] but with a better lateral resolution.

Even for smaller objects (such as coins), which might be analysed as a whole in a conventional XRF instrument, the use of a small beam instrument offers advantages as only a small area of the (altered) surface needs to be removed in order to expose the underlying original material. A small x-ray beam obviously also permits the analysis of an object at various locations, e.g. to verify that all parts of a statue are made of the same material, or to investigate the homogeneity of the material used. XRF on curved or otherwise non-flat surfaces can lead to errors in quantification (especially for metallic materials);[8] with a small beam, it is in general easier to select locations on an object which resemble more closely to the ideal, flat and polished surface normally required for reproducible quantitative measurements.

A recent direction in $\mu$-XRF instrument development is the construction of compact small-beam instruments, consisting for example of an air-cooled mini-focus x-ray tube, a compact optical element for beam focusing/collimation and a Peltier-cooled energy-dispersive detector. The availability of such instruments, offering beams of 50–200 μm cross-section, will be very useful for the *in situ* investigation of archaeological and artistic materials, i.e. in the museum, gallery or archaeological site where they are normally located.

In this paper, after briefly describing the instrumentation employed for the investigations, a number of case studies highlighting the above-outlined types of investigations are outlined. Most of there were performed at the authors' laboratories; the results of a number of other studies in the same field, taken from the literature, are briefly cited in order to complete the overview.

## MICRO-XRF EQUIPMENT EMPLOYED FOR INVESTIGATIONS IN ART AND ARCHAEOMETRY

### Synchrotron micro-XRF instrumentation

**Polychromatic excitation at Hasylab Beamline L.** The experimental set-up used for synchrotron micro-XRF measurements installed at Hasylab Beamline L in depicted schematically in Fig. 1(a). Figure 2(a) shows the energy distribution in the white beam, produced in a bending magnet source, as seen through a $10 \times 10$ μm pinhole, positioned at 20 m from the synchrotron ring. As can be seen in Fig. 2(a), bending magnets of the DORIS storage ring produce a white spectrum which contains appreciable amounts of very energetic photons (above 60 keV), which is not the case with many other synchrotron facilities, e.g., the NSLS (National Synchrotron Light Source, Upton, NY, USA).

The beam that originates from the storage ring is first collimated down to ca $100 \times 100$ μm$^2$ by motorized cross-slits before entering the capillary. The latter is mounted on a motorized $XY\theta\varphi$ stage for alignment to the beam. Usually, straight borosilicate glass capillaries of 10–50 μm i.d. are employed for microbeam formation;[9] the capillary–sample distance is typically of the order of a few millimetres. Through repeated total external reflection on the inner walls of the tube, x-ray photons are transported along the length of the tubes; thus, straight capillaries act as effective apertures over a wide energy range. Since metal pinholes or cross-slit systems are not effective in collimating the high-energy portions of the white beam to a micro-spot with well-defined shape, straight capillaries are employed for this purpose. However, these devices do not 'concentrate' the x-ray beam. If ellipsoidal lead-glass capillaries are employed,[10] the capillary is positioned is such a way that its tip is about 0.5–1 mm away from the sample surface. Inside ellipsoidal capillaries, the x-ray photons are subject to only one or a few reflections and part of the radiation is focused in this manner. The sample

Copyright © 2000 John Wiley & Sons, Ltd. 

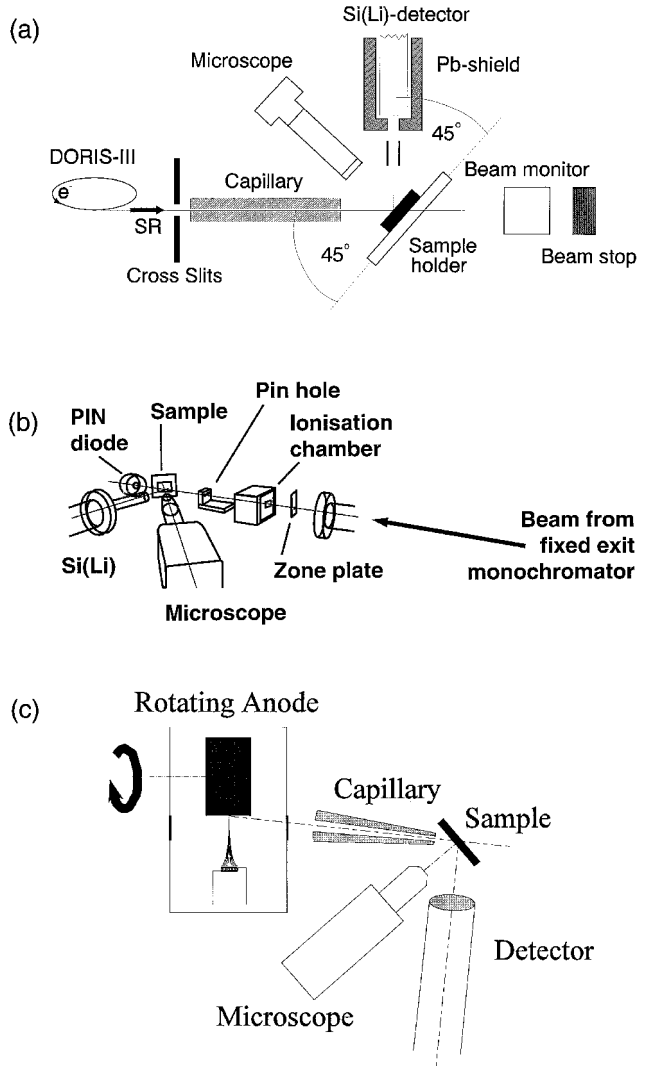


**Figure 1.** Schematic diagram of (a) the polychromatic $\mu$-SRXRF spectrometer installed at Beamline L, Hasylab (DORIS III storage ring), Hamburg, Germany, (b) the monochromatic $\mu$-SRXRF facility at Beamline ID22, ESRF, Grenoble, France and (c) the laboratory $\mu$-XRF spectrometer of the University of Antwerp, Belgium, based on a rotating anode generator and capillary optics.

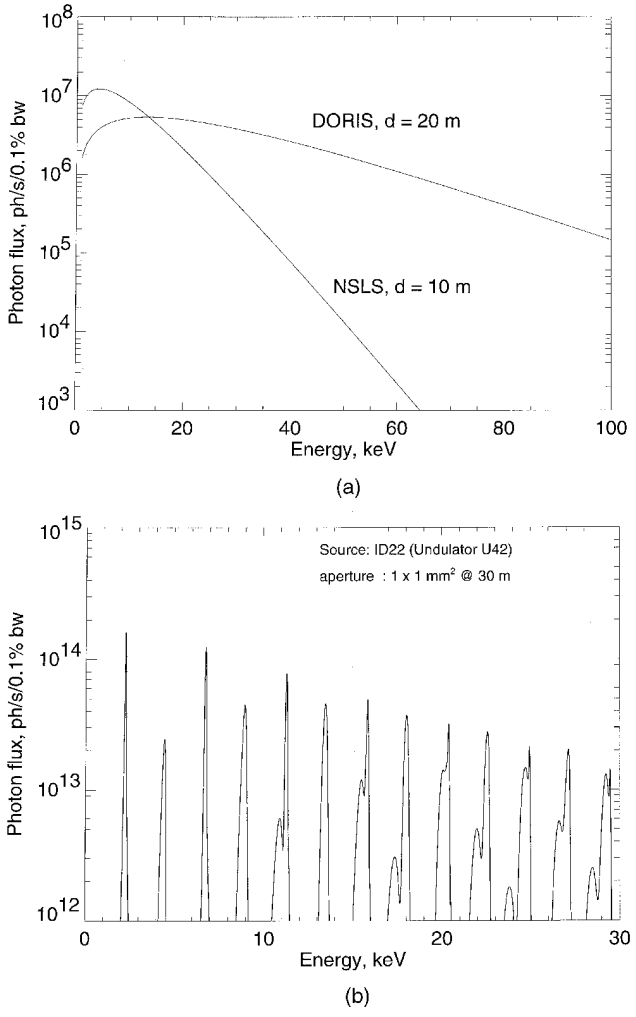


**Figure 2.** (a) Energy distribution in the white beam used for sample excitation at Beamline L, Hasylab (DORIS storage ring), Germany; for comparison, the white spectrum produced by the National Synchrotron Light Source (NSLS, Upton, NY, USA) is also shown. (b) Typical energy spectrum emitted by the undulator source at the ID22 Beamline, Grenoble, France. bw = Bandwidth.

itself is mounted on a motorized $XYZ\theta$ stage, allowing it to be moved in increments of 1 μm and 0.1°. The sample surface plane is vertical and oriented at 45° to the incoming microbeam and is also in the focal plane of the long-distance optical microscope which is placed horizontally. Fluorescent signals are detected by an HPGe (high-purity germanium) solid-state detector; the latter is located at a distance of 5–7 cm from the sample and is shielded by a Ta/Pb enclosure. The detector collects the fluorescent and scattered radiation in a solid angle of ca 0.001 sr. The vertical position of the detector is such that it is exactly in the (horizontal) plane formed by the storage ring and the microbeam. Since the HPGe detector is oriented at 90° to the microbeam in the plane of maximum linear polarization, the XRF spectra which are collected in this way feature optimum peak-to-background ratios as the scatter-induced continuum background is reduced in intensity.[11] Behind the sample, an ionization chamber is placed to monitor the transmitted beam intensity; a similar monitor can be placed in the beam path between slits and capillary [not shown in Fig. 1(a)].

During conventional $\mu$-XRF measurements, involving point analyses, line scans or two-dimensional (2D) mapping, the sample is moved through the beam by means of the motorized stage (in the $XYZ$ directions) so that the appropriate locations on the surface are irradiated; the rotation stage ($\theta$ stage with vertically oriented rotation axis) normally is useful only during tomography-type measurements.[12] Correlated stage movement and spectrum acquisition allow the collection of $n_x \times n_y$ individual XRF spectra ($n_x$, $n_y$ = number of pixels in horizontal and vertical directions of the image, respectively) which during or after the acquisition can be processed to yield (net) elemental maps, line profiles or area/phase-specific sum spectra of the irradiated material. By means of appropriate calibration models, the latter can be converted into quantitative images or local composition values.[13]

The analytical characteristics of this facility have been extensively described elsewhere.[14] A special feature of this

Copyright © 2000 John Wiley & Sons, Ltd.

experimental facility is the fact that K-line XRF measurements can be performed on the chemical elements ranging from K ($Z = 19$) to Pb ($Z = 82$) because of the high-energy components of the white beam. In the transition metal range, femtogram-level absolute minimum detection limits (MDLs) in thin samples and ppm-level relative MDLs in thick organic or silicate-based samples are obtained whereas for the lanthanides, equivalent values are situated around 10 fg and 5–10 ppm, respectively, within a 1000 s irradiation time.[15] In addition to the high intensity of the synchrotron beam, the high sensitivity over an extended element rage is also the consequence of the fact that in SRXRF spectra, a reduced background level is observed. This is the result of the polarized character of the radiation and the fact that the XRF is detected in the plane of the synchrotron ring (see Ref. 16 for details). A disadvantage of the use of the strongly penetrating primary and fluorescent radiation is that the analytical signals in thick samples can originate from extensive depths [e.g. for rare earth elements (REE) this can be up to several millimetres in glass samples], thereby reducing the effective lateral resolution of the technique in one direction. This blurring effect can be avoided by employing thin samples.

**Monochromatic excitation at the ESRF Beamline $\mu$-FID22.** ESRF Beamline ID22 is an undulator beamline which means that instead of a continuous energy distribution such as shown in Fig. 2(a), only photons within specific energy bands are produced. These relatively narrow (a few hundred eV wide) energy ranges are called undulator harmonics. Undulators are periodic multipole magnetic structures of which the magnetic field strength can be adjusted to suit the users' needs. Figure 2(b) shows the energy spectrum of the undulator device at ESRF ID22. By changing the undulator gap width, the energy of the harmonics can be adjusted so that the output flux of an undulator in a specific energy range can be optimized. In view of their quasi-monochromatic nature, undulator sources are therefore more suitable for performing micro-XRF experiments involving monochromatic primary microbeams, of which the energy can optionally be tuned. In Fig. 1(b), a schematic diagram of the experimental arrangement is shown. At ESRF ID22, a fixed-exit monochromator can be employed to select a very narrow energy band ($\Delta E/E \approx 10^{-4}$) from an undulator peak. Via the monochromator settings, the energy of the primary beam can be scanned in a narrow range around the absorption edge of an element of interest in order to perform combined $\mu$-XRF and $\mu$-XANES (x-ray absorption near-edge spectroscopy). During a XANES experiment, the energy of the primary beam is scanned in eV or sub-eV steps around an absorption edge of a particular element while the absorption and/or the resulting flux of fluorescent radiation is measured. Since the exact location and shape of the absorption edge changes as a function of the oxidation state and chemical environment of the element in question, this type of measurement can reveal information on the local oxidation state of that element. After the monochromator, the beam is focused on to the sample by means of a Fresnel lens;[17] an additional pinhole is used to reduce the scatter background in the sample area and to define the beam in the horizontal direction. In this manner, a beam spot of $3 \times 5$ μm$^2$ can be obtained. Because the monochromator is of the fixed-exit type, during XANES energy scans, the position and width of the microbeam on the sample do not change. This means that completely independently of each other, the irradiation position and primary beam energy can be user manipulated in a reproducible manner, permitting $\mu$-XANES imaging. Such experiments involve normal $XY$ scanning of the sample at various primary energies, as explained below (see Fig. 14).

## Laboratory $\mu$-XRF equipment

**Monocapillary-based $\mu$-XRF instrument.** A schematic layout of a laboratory-scale $\mu$-XRF spectrometer is shown in Fig. 1(c). In principle, the basic layout is very similar to that of the polychromatic synchrotron instruments described above. A glass capillary is used for concentrating the radiation generated by a rotating anode source on to the sample which is mounted on an $XYZ\theta$ stage. The sample is viewed with an optical microscope using long working distance lenses. Elemental maps can be recorded by moving the sample through the microbeam and collecting an ED-XRF spectrum at each location. Since the efficiency with which conical and ellipsoidal capillaries concentrate x-rays decreases with increasing photon energy, often Cr and/or Cu tubes are employed as x-ray sources in these instruments. With these tubes, beam sizes down to 5–10 μm can be employed with good sensitivity.[8] When Mo or Rh anodes are used, the smallest beam size offering a sufficient photon flux is in the range 20–40 μm. When comparing the elemental yields (in counts s$^{-1}$ pg$^{-1}$) from this laboratory set-up and the instrument at Hasylab Beamline L, a reduction by a factor 10–30 in the elemental range Ca–Zr is noted. This means that all measurements take a long time to finish and automated overnight measurements are the rule rather than the exception for image acquisition. Absolute MDL values in thin samples are situated in the 1–10 pg range as opposed to femtogram levels with synchrotron instrumentation. In addition, the advantages of the use of linearly polarized synchrotron radiation with respect to spectral background reduction are not present here so that also in relative terms, the sensitivity is lower: in high scattering materials, typical detection limits in the 10–30 ppm range are obtained.

**Polycapillary-based $\mu$-XRF spectrometer.** The polycapillary based $\mu$-XRF spectrometer for which some results will be discussed below consists of a Kevex PXS4 mini-focus Mo-tube x-ray tube (70 W maximum power, 250 μm anode spot), an $XYZ\theta$ sample translation/rotation stage, an optical microscope and an Si(Li) detector. The distance from the impact point of the electrons on the anode to the Be window of the tube is ca 2.0 cm; the emerging x-rays are focused by a polycapillary lens which is contained in a cylindrical brass holder; the latter is mounted on a five-axis gimbal lens holder (Newport M-LP-05B). The receiving end of the capillary is placed at a distance that maximizes the transmission through the lens. Fluorescent radiation is detected with a 30 mm$^2$ Canberra Si(Li) detector (180 eV resolution at Mn K$\alpha$) having a 2.5 cm

Copyright © 2000 John Wiley & Sons, Ltd. 

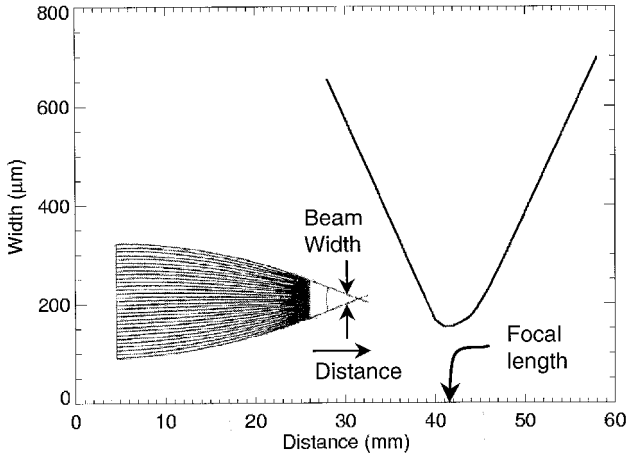


**Figure 3.** Focusing characteristics of a polycapillary lens with output focal length of 4.5 cm. The beam width is the smallest (ca 150 μm) at a distance of ca 42 mm from the end of the capillary lens.

diameter end-cap. In this case, a polycapillary lens manufactured by the Institute for Low Energy Physics (Bejing Normal University, Beijing, China) was employed. As shown in Fig. 3, this lens focuses x-rays into a focal spot of ca 150 μm at a distance of 4.5 cm from its output end. With lenses with shorter focal lengths (of ca 15 mm), focal spot sizes down to 50 μm were obtained. The most striking advantage of using polycapillary lenses is that a large fraction of the cone of radiation that emerges from the x-ray tube is collected by the lens. However, since the lens mostly consists of strongly curved capillary tubes, its efficiency is must higher at low energy (below 10–15 keV) than in the range 15–25 keV. Accordingly, this optical element strongly influences the excitation spectrum that finally impinges on the sample surface.[18] In the 5–10 keV region of the spectrum, this gives rise to a high scatter background but also to a high excitation efficiency. As a result, although a highly intense sub-millimetre beam can be created in this way, the relative detection limits of this instrument for transition metals in glass are situated at the 30–100 ppm level. In metallic matrices such as bronze or silver (strong matrix lines and strong self-absorption), the MDL values are around the 100 ppm level.

## TRACE ELEMENT FINGERPRINTING

### Trace analysis of ancient glass

Although not so frequently encountered at archaeological sites as metallic and stone artifacts, the use of objects in silicate glass has been known since prehistoric times. Specific glass compositions can be associated with particular time periods and geographical locations.[19] It is recommended to employ a microanalytical method to determine the chemical compositions since only a minute piece of material is required for analysis. If the analyses are performed on fragmented objects (as is mostly the case for glass vessels found during excavations), sampling of small fragments of the material normally does not pose problems. EPXMA can be used for major/minor element analysis down to ca 0.1% (w/w) (see, e.g., Ref. 20) but does not provide information on traces. By performing $\mu$-XRF measurements on the same samples, the quantitative trace element signature of the objects can be determined. In this manner, both techniques are employed in a complementary manner since $\mu$-XRF is not able to provide information on the low atomic number elements such as Na and Mg.

On the other hand, for the analysis of intact (museum) pieces, sampling usually is not possible, desired or permitted and non-destructive methods that are able to analyse large objects with spatial resolution on the sub-millimetre scale are preferable, such as external beam PIXE. Since most $\mu$-XRF spectrometers operate in ambient air, they can usually be employed for the local analysis of macroscopic objects without great difficulty.

**Roman glass.** Glass from the Roman period (1st–6th centuries) has a low magnesium/low potassium soda-lime composition,[21] typically consisting of ca 66–72% $SiO_2$, 16–18% $Na_2O$ and 7–8% CaO. For Roman glass, the major element composition can only be used to verify that a particular fragment or object is genuinely Roman, but usually does not convey other information. The reason for this is that all the glass found throughout the Roman Empire from the 1st to the 6th century features a nearly identical major element composition. As an example, Table 1 gives the average composition of a number of glass fragments found at the Khirbet Qumrân site in Israel;[22] in total, about 100 different objects of various shapes were found at this site and analysed. In Fig. 4 the dendrogram obtained by hierarchical cluster analysis of the elemental data is shown. Two large groups may be discerned, of which the largest may be further subdivided. The average composition of the groups is given in Table 1. Comparison of the average compositions reveals a significant difference only in the CaO content (8% for group 1 and 5% for group 2), which may be related to the origin of the natron (an $Na_2CO_3$-rich deposit used a raw material for the glass making).

To verify the compositional homogeneity of the glass in both groups, in addition to EPXMA measurements, the trace compositions (down to the 1–10 ppm level) of the fragments were determined by $\mu$-SRXRF. Details on the calibration procedure applied and on its accuracy can be found elsewhere.[23] When also the trace concentrations are employed for performing a cluster analysis, the two groups previously found are obtained, except that within group 1 (Ca-rich), a subgroup containing five objects with a much lower Sb concentration is identified (group 1b). The distinction between groups 1 and 2 can now be made clearer since in the trace-element fingerprint, significant differences in the average concentrations of Cu, Sn, Pb and Sb are found. All these elements are associated with the colour of the glass: Cu, Sn and Pb probably originate from bronze chips which may have been intentionally added to the glass melt to give it a green colour; Sb was used to decolorize the glass and give it a clear, transparent appearance. Together, major and trace-element data indicate that the entire series of ca 100 glass vessels found at the Qumrân site originated from one or two workshops and were probably purchased together. This information supports the hypothesis[24] that at this site perfumes and ointments were manufactured on a large

Copyright © 2000 John Wiley & Sons, Ltd. 

**Table 1. Compositional categories found in a series of Roman glass samples from Qumrân, Israel[a]**

| Constituent Concentration (%, w/w) | Group 1a ($n = 45$) | Group 1b ($n = 5$) | Group 2 ($n = 9$) |
|---|---|---|---|
| $Na_2O$ | $16.38 \pm 0.4$ | $16.28 \pm 0.6$ | $17.2 \pm 0.35$ |
| MgO | $0.23 \pm 0.13$ | $0.07 \pm 0.13$ | $0.01 \pm 0.01$ |
| $Al_2O_3$ | $2.5 \pm 0.1$ | $2.4 \pm 0.1$ | $2.4 \pm 0.3$ |
| $SiO_2$ | $69.5 \pm 0.6$ | $70.9 \pm 1.6$ | $71.7 \pm 0.4$ |
| $P_2O_5$ | $0.08 \pm 0.04$ | $0 \pm 0$ | $0.02 \pm 0.04$ |
| $SO_3$ | $0.16 \pm 0.11$ | $0.2 \pm 0.07$ | $0.17 \pm 0.07$ |
| Cl | $0.82 \pm 0.07$ | $1.06 \pm 0.05$ | $1.16 \pm 0.05$ |
| $K_2O$ | $0.84 \pm 0.06$ | $0.61 \pm 0.11$ | $0.58 \pm 0.12$ |
| CaO | $8.41 \pm 0.6$ | $7.54 \pm 0.42$ | $5.52 \pm 0.6$ |
| $TiO_2$ | $0.05 \pm 0.04$ | $0.02 \pm 0.02$ | $0.04 \pm 0.04$ |
| MnO | $0.43 \pm 0.06$ | $0.09 \pm 0.09$ | $0.84 \pm 0.13$ |
| $Fe_2O_3$ | $0.52 \pm 0.06$ | $0.39 \pm 0.13$ | $0.33 \pm 0.04$ |
| | Concentration (ppm, w/w) | | |
| $Cr_2O_3$ | $12 \pm 12$ | $9 \pm 8$ | $23 \pm 27$ |
| NiO | $7 \pm 5$ | $8 \pm 8$ | $15 \pm 7$ |
| CuO | $209 \pm 95$ | $83 \pm 137$ | $50 \pm 43$ |
| ZnO | $35 \pm 19$ | $18 \pm 13$ | $26 \pm 7$ |
| Br | $7 \pm 11$ | $7 \pm 4$ | $8 \pm 7$ |
| $Rb_2O$ | $14 \pm 4$ | $13 \pm 3$ | $12 \pm 3$ |
| SrO | $637 \pm 145$ | $570 \pm 137$ | $534 \pm 130$ |
| $Y_2O_3$ | $9 \pm 2$ | $8 \pm 3$ | $6 \pm 1$ |
| $ZrO_2$ | $79 \pm 17$ | $59 \pm 15$ | $63 \pm 16$ |
| $Mo_2O_3$ | $3 \pm 2$ | $0 \pm 0$ | $3 \pm 1$ |
| $SnO_2$ | $113 \pm 49$ | $52 \pm 21$ | $56 \pm 34$ |
| $Sb_2O_5$ | $354 \pm 190$ | $1 \pm 1$ | $29 \pm 31$ |
| BaO | $234 \pm 127$ | $151 \pm 92$ | $151 \pm 59$ |
| PbO | $156 \pm 64$ | $13 \pm 9$ | $17 \pm 14$ |

[a] Uncertainties represent the standard deviation of concentration in each group.

scale, requiring large numbers of small glass vessels as containers.

Three hypotheses have been formulated to explain the exceptional chronological and geographical constancy in the composition of Roman glass:[25–27]

(a) all the Roman glass was manufactured in one or a few sites (primary workshops) in the Middle East (Syria or the northern part of Egypt) and shipped in ingots all over the Empire for remelting and modeling into various shapes (secondary workshops);
(b) glass manufacture was strictly controlled and was always done with the same (high-quality) raw materials; and
(c) extensive recycling of glass took place.

In order to evaluate these hypotheses, a systematic study involving five Roman sites in Belgium (Tongeren, Oudenburg), The Netherlands (Maastricht), France (Rouen) and Germany (Cologne, Trier) and the analysis of over 250 glass fragments was undertaken; see Ref. 28 for details of the sites and the analytical results obtained. From these data, several conclusions could be drawn:

- with the exception of minor and trace elements related to the colour of the glass (Al, Mn, Fe, Cu, Zn, Pb, Sn, Sb),[29] all investigated glass objects show the same composition; This indicates that over a period of 600 years the glass was always prepared with the same or very similar raw materials;
- whereas in the 1st–4th centuries Sb was used as a glass decolorizer, in later periods it was no longer used and was replaced by Mn;[30,31]
- glass from the later period (5th–6th centuries) in general contains a higher content of trace constituents than the earlier glass;
- at various sites, indications are found of the intentional use of brass (Cu–Zn) or bronze (Cu–Sn–Pb) or related ores for colouring the glass.[31]

These observations in general support hypothesis (a) and disprove hypothesis (b), while in the later centuries evidence of extensive recycling, together with certain changes in glass technology, is also found.

In this particular case, the ability of $\mu$-SRXRF to extract trace element data on medium to heavy metals (Fe–Ba) down to the ppm level from minute glass fragments was found to be very valuable.

**Post-medieval glass.** The complementary nature of EPXMA and $\mu$-SRXRF is also illustrated in Fig. 5, which shows major and trace element scatter plots of a series of different 16th–17th century soda-lime glass fragments excavated in various sites in the historic centre of Antwerp, Belgium.[32] Figure 5(a) shows a few typical shapes of post-mediaeval soda-lime vessels. In contrast to the Roman period, during the Mediaeval and post-mediaeval period, glass of widely different composition is used. In addition to (usually colourless) soda-lime glass, green forest glass (containing no $Na_2O$ but 20–25% CaO and 5–10% $K_2O$) and yellowish green fern glass (with, e.g., 10–15% $K_2O$ and 10% CaO) are frequently encountered[33] in addition to mixtures of the above glass types. Because of these large differences in major composition, trace element data are not directly required to obtain information on the general origin of the glass. However, within each of the large compositional groups, information on minor/trace constituents such as Sr, Rb, Zr, Sn, Sb and Pb was found to be useful for making more subtle distinctions (see Ref. 32 for details). As an example, in Fig. 5(b) the $Na_2O$ vs CaO plot of major elements concentrations found in a series of 250 post-mediaeval soda-lime vessels excavated in Antwerp reveals five distinct groups. Two groups (labelled 'Antwerp Cristallo' and 'Vitrum Blanchum') show major compositions nearly identical with those of established glass compositions fabricated in Venice in this period,[34] suggesting that these objects might be imported; three other groups appear to be specific for the Antwerp production. At first sight, the proportion of the Cristallo and Vitrum Blanchum groups appears to be important among the Antwerp finds; this is surprising since in other studies on glass fragments excavated in cities such as London and Amsterdam, only very rarely was glass having the specific 'Cristallo' composition found. In order to investigate in greater detail whether the Antwerp Cristallo objects were indeed made with the same raw materials as genuine Venetian vessels (very pure silica pebbles and purified ashes of specific marine plants), trace analysis of the same minute glass fragments (previously used for major element analysis by EPXMA) was performed by SRXRF at the Hasylab Beamline L facility. In addition, a number of glass fragments excavated in the Venice Lagoon were put at our disposal by M. Verita and P. McCray and also analysed as a reference. Inspection of the trace element data revealed

Copyright © 2000 John Wiley & Sons, Ltd.

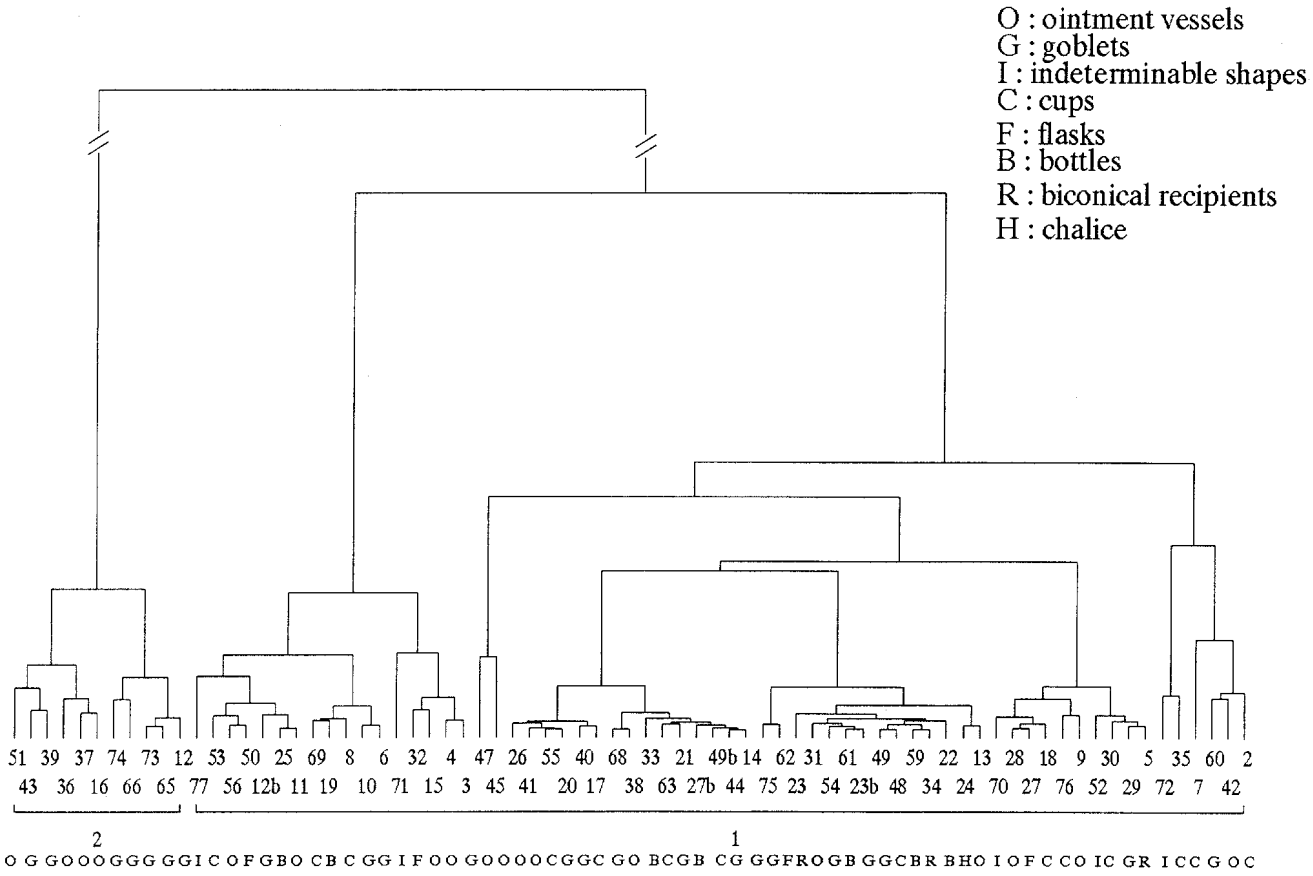


**Figure 4.** Dendrogram obtained by clustering the major element data obtained from a number of the Qumrân glass artefacts. Two large groups (1 and 2) are present; in their major composition, they differ significantly only in Ca content. Sample identification numbers and vessel types are shown below the dendrogram.

that especially the Zr content of the glass can be used to distinguish between the glass vessels of Venetian and non-Venetian origin found in Antwerp: whereas the majority of the Antwerp finds feature a $ZrO_2$ content between 40 and 100 ppm, the truely Venetian fragments and a very limited number of Antwerp finds show a significantly lower $ZrO_2$ concentration in the range 10–20 ppm.

The graph in Fig. 5(c) illustrates the usefulness of trace element data for making subtle compositional distinctions between cultural heritage artifacts of different provenance.

By making use of the LURE microprobe, Figueiredo *et al.*[35] characterized rare Mediterranean elongated glass beads composed of five identifiable successive concentric layers of different colours: white, red, green and blue.

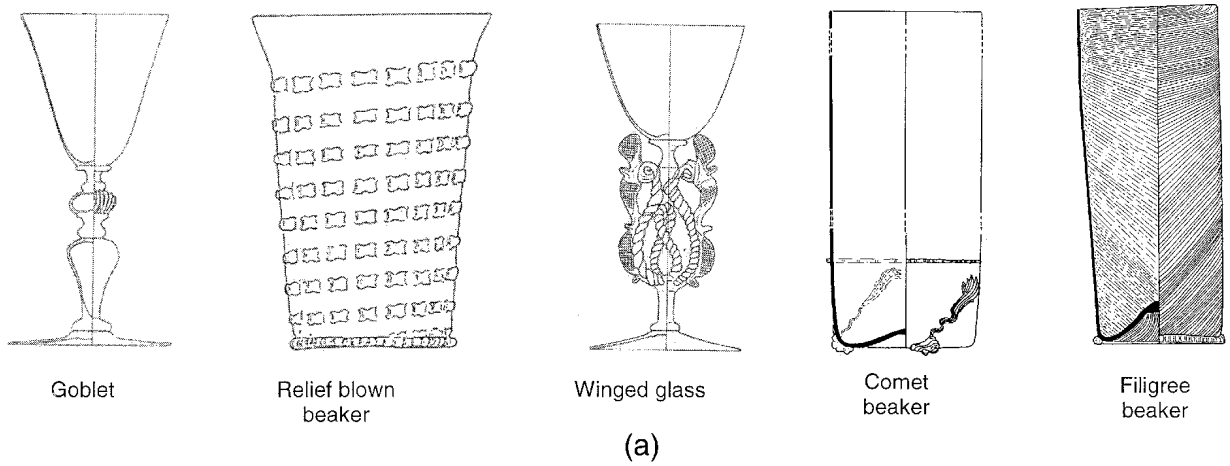


**Figure 5.** (a) Typical shapes, (b) $Na_2O/CaO$ (%, w/w) and (c) Zr/Sr concentration scatter plots (ppm) of different types of 15–17th century glass objects excavated in Antwerp, Belgium. The relative uncertainty is ca 5% on the major element concentrations is and ca 10% on the trace concentrations. Circled fields in denote the majority of the genuinely Venetian 'Cristallo' and 'Vitrum Blanchum' objects.

Copyright © 2000 John Wiley & Sons, Ltd. 

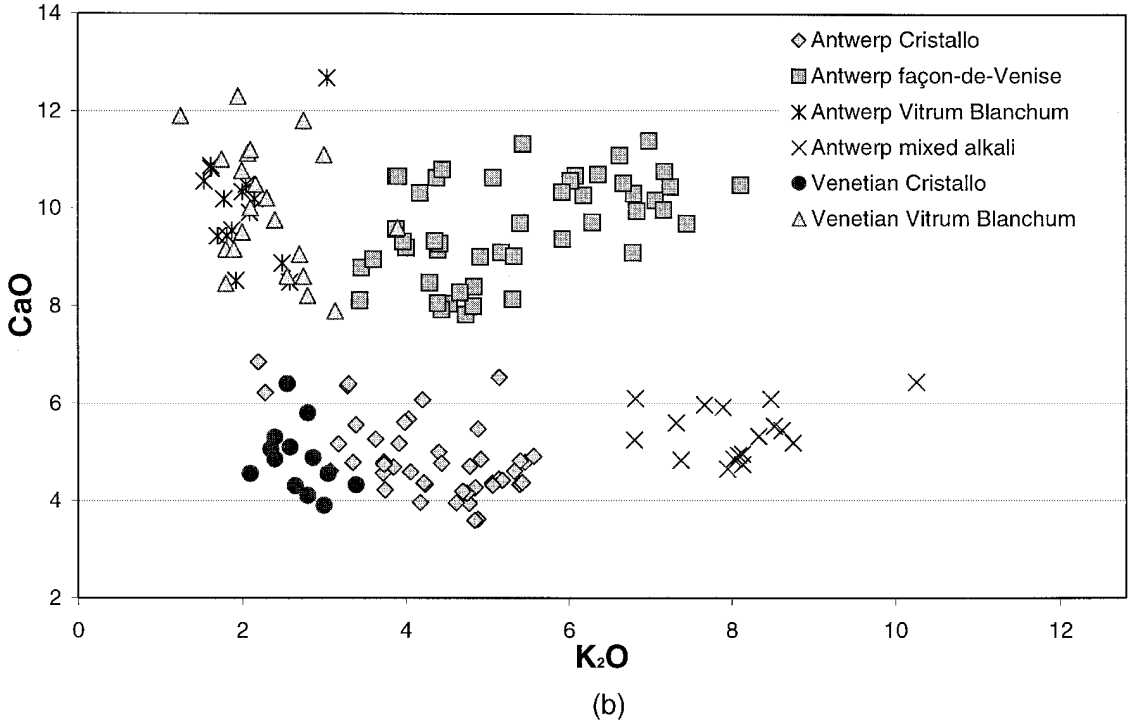


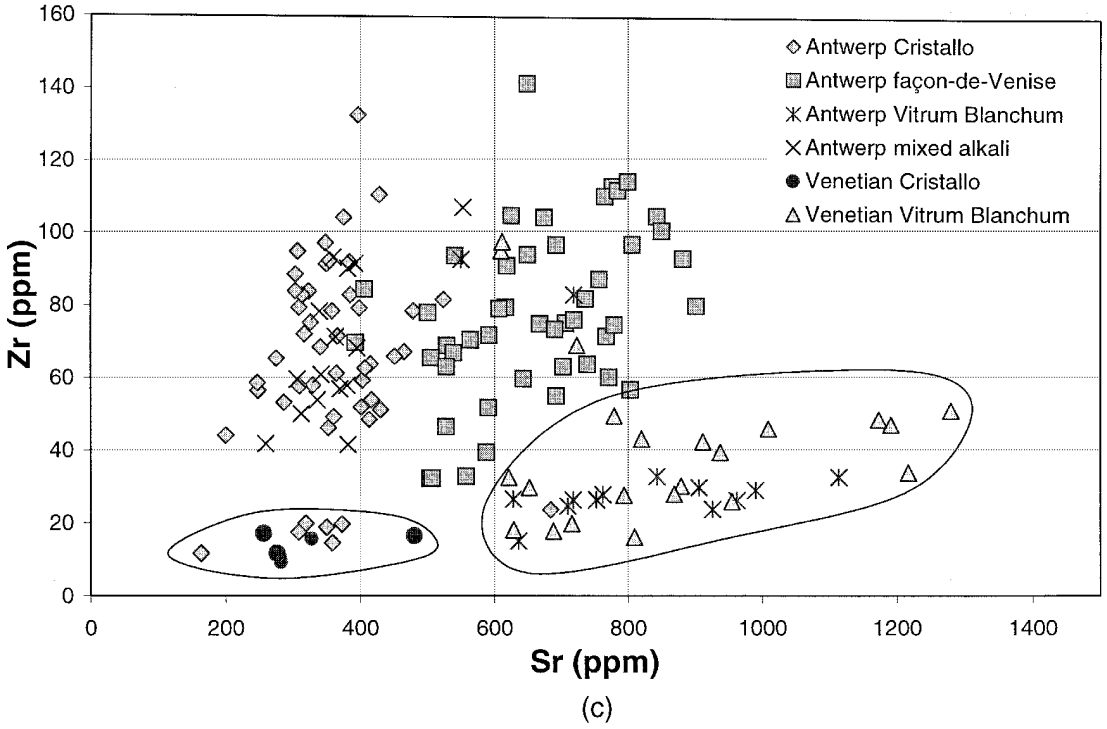


**Figure 5.** (*continued*).

They performed measurements at 8 and 21 keV primary energy to optimize the excitation conditions for a large range of chemical elements. The incident synchrotron radiation was kept parallel to the bead axis to ensure that all glass layers could be analysed separately. The white glass layers were opacified by means of Sn. Independently of the colour, in each of the coloured layers significant amounts of Cu and Pb were found, although the outer green layer is poorer in Pb and richer in Cu, K and Ca relative to the other layers. The white and bluish layers contain more Zn. Possibly the chemical state of Cu (the only chromophore ion present) and therefore the redox conditions during the manufacture of the glass determined the colour of the glass. Additional research involving $\mu$-XANES to determine the oxidation state of Cu in the different layers is currently under way.

## Analysis of inks

The ability to analyse artifacts in an air environment (i.e. without requiring vacuum) and in a non-destructive

Copyright © 2000 John Wiley & Sons, Ltd. 

manner makes $\mu$-XRF especially suitable for the analysis of inks or other types of metal-containing pigmented materials deposited on fragile and easily damaged materials such as paper or parchment.

**Trace analysis of early printing inks.** Knöchel and Haller[36] and Mommsen *et al.*[37] compared the concentrations of Cu and Pb in ink of the Gutenberg Bible with that of other early single leaf copies and books. The pioneering work with PIXE by Cahill and co-workers[38,39] identified the analysis of ink as a new research tool for the history of early printing (from the second half of the 15th century).[40,41] It is assumed that each printer/printing office can be recognized by a specific ink preparation as reflected in the trace element signature of the dried ink. The recipes for the ink were kept as a secret; in the 15th century, not a single specification of composition is documented.[42]

Mommsen *et al.*[37] employed a $0.5 \times 1$ mm polychromatic x-ray beam derived from the synchrotron storage ring ELSA (Bonn, Germany) for irradiating single leaves of early 15th century printed paper. Ink and paper of 22 different works from different locations in Germany, Italy and Switzerland were analysed. The energy deposited in the paper during the measurements (300 s) was estimated to be ca 15 $\mu W\ cm^{-2}$, i.e. about a factor of 70 lower than bright sunlight.

Comparison of the spectra from paper and paper–ink combinations from page II, 316 of the single leaf 42-line Gutenberg Bible revealed that Ni, Cu and Pb are present in the ink at concentration levels of a few tens of $\mu g\ cm^{-2}$, whereas K, Ca, Ti, Mn, Fe and Zn originate from the paper base.

In six of the 22 leaves, printed areas could not be distinguished from blank areas, suggesting that the corresponding inks were prepared from mainly C-bearing material such as lampblack or soot.[42] In some of the other inks, in addition to Ni, Cu and Pb, also K, Ca and Fe were present. On all pages analysed except the Gutenberg leaf, the same ink composition on the recto and verso sides were found. On the recto side of the Gutenberg B-42 leaf, the ink thickness was ca three times larger than on the verso side, although both sides show the same Cu/Pb and Ni/Pb ratios ($1.0 \pm 0.5$ and $0.007 \pm 0.003$, respectively). For the same page (II, 316) of the Harvard Gutenberg Bible, by means of PIXE recto and verso Cu/Pb ratios of $1.15 \pm 0.05$ and $1.44 \pm 0.07$, respectively were reported.[37–40]

For three specific printers, the constancy of their ink composition over large time intervals was tested by analysing leaves of several books produced by them. They appear to have changed the composition of their inks fairly frequently. It therefore appears difficult to establish a definite trace element pattern specific for one printer. When only the trace elements which occur in the ink alone (and not in the paper) are considered, only Pb and Cu concentrations can be used for distinguishing between early printers.

As a result of this study, Mommsen *et al.*[37] concluded that a systematic investigation of the ink composition in works printed 10–15 years after Gutenberg's first Bible edition is needed to learn more about the early recipes for ink preparation and to find specific reasons for the presence of metallic impurities in the ink. The SRXRF method was found to be suitable for non-destructive measurements on this fragile type of material and appropriate for performing the large number of measurements required to reveal systematic trends in the composition of paper and inking.[37]

**Visualization of invisible handwriting on historic documents.** In addition to SR-XRF, laboratory $\mu$-XRF is also an excellent technique for the analysis of valuable documents, for example to determine their authenticity. Typically, different inks, while having the same visible appearance, will have different chemical compositions. Larsson[43] and Stocklassa and Nillson[44] described analysis by $\mu$-XRF of a 500-year-old Swedish possession letter (dated April l, 1499). The document, a sales contract for an estate, showed signs of alterations. It was suspected that the alteration was made in the 1530s, when the Swedish king restored land back to certain nobles, who previously had been stripped of their estates by an earlier ruler. Although alteration was suspected by visual inspection (the original name of the owner had been removed by scraping), the original text was unreadable. By employing $\mu$-XRF-generated Zn maps (a trace constituent of the original ink), the original name could be established, however. In Fig. 6, $\mu$-XRF scans of Ca and Zn are shown across a selected area of the parchment. In the Ca map, the (falsified) visible text can be seen, featuring the family name 'Gäsmestad i Böre'; in the Zn map of the same area, however, a completely different text reading 'Bøtinge i Asbo' becomes visible. Obviously, the forger used different ink for the alteration, accounting for the change in chemical makeup.

## Local analysis of macroscopic objects

**Enamel decorations.** An area in which authentication of art objects is of considerable (economical) interest in that of Oriental china ware. Up to the 17th century, high-quality porcelain was exclusively manufactured in China and Japan and imported china ware was highly valued and expensive. In the later periods an extensive production system of counterfeit Chinese and/or Japanese porcelain both in Europe and in Asia came into existence. Some of the reproductions are very sophisticated and cannot be easily distinguished from the original counterparts by visual inspection alone.

Objective ways of distinguishing between original period and more contemporary reproductions have until now focused on the porcelain base material itself.[34,35] A complementary approach is to consider the composition of the enamel paints used to decorate the objects. In view of the size and shape of the pieces, this type of analysis is difficult to perform using scanning electron microscopy equipped with energy-dispersive X-ray detection (SEM–EDX), while the intricacy of the decoration patterns usually precludes the use of conventional XRF. However, $\mu$-XRF analysis of individual decorations is feasible.

As detailed earlier,[9] by employing a monocapillary-based instrument, it is possible to record large-scale $\mu$-XRF maps of these decorations and to determine which transition elements (e.g. Mn, Fe, Cu) were employed to colour the PbO-based enamel paint. As an example, Fig. 7 shows large-scale ($4 \times 4$ cm) x-ray maps of a painted figure on the vase shown in Fig. 8. To record these images, the vase was mounted on a rotation table so that surface of

Copyright © 2000 John Wiley & Sons, Ltd.

**Figure 6.** Elemental maps of several elements obtained by $\mu$-XRF analysis of an area on a Swedish property deed (photograph courtesy of A. Rindby).

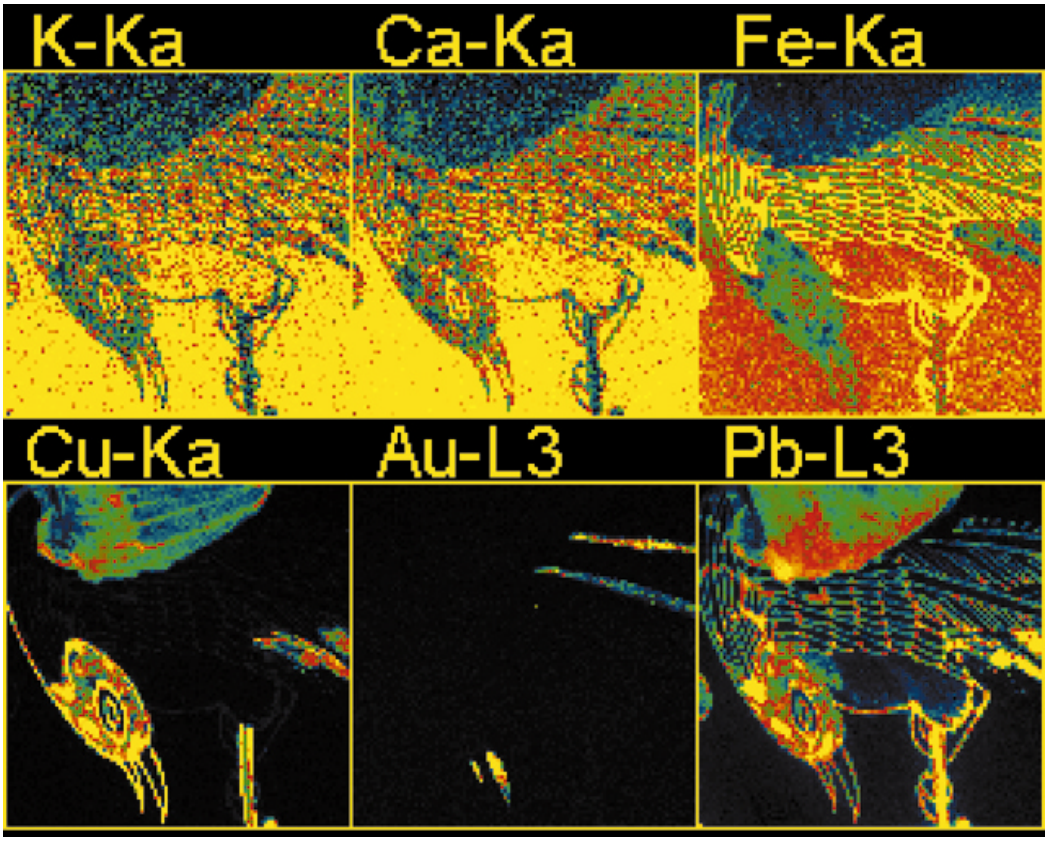


**Figure 7.** Large-area elemental maps obtained by translating/rotating a Japanese 18th century vase through a 15 $\mu$m beam. The area scanned is 4 $\times$ 4 cm.

Copyright © 2000 John Wiley & Sons, Ltd. 

the object maintained a constant distance to the capillary tip and detector. The various types of enamel paint [based on lead oxide as fluxing agent and coloured with transition metals such as Fe (red), and Cu (green/black)] can be clearly distinguished, in addition to the presence of decorative gold details. The K and Ca signals from the feldspar glaze are absorbed by the enamel paint. It appears that originally these vases were only decorated with a few simple blossoms (see Fig. 8, rightmost flower) but that later more decorations were added using enamel paint of similar colour. It was possible to distinguish between originally present and add-on decorations of the same colour on the basis of the local XRF spectra.[9]

**Coins and statues.** Brissaud *et al.*[45] compared SRXRF (as implemented in the LURE $\mu$-XRF facility) at 17 and 35 keV excitation energy, PIXE and neutron activation analysis (NAA) for the analysis of gallic coins having a Cu–Ag–Sn matrix composition. The aim of the investigation was to make a comparison of the data obtained from the surface of the coins with SRXRF and PIXE to that obtained from the bulk of the samples with NAA. At 17 keV, in this matrix, the 1/e penetration depth of x-ray photons is 30 μm and at 35 keV it is 70 μm; 2 MeV protons penetrate about 12 μm in this material. Some of the quantitative data are shown in Fig. 9. Few differences in the surface concentrations using the three beam methods were observed; however, a large discrepancy with the NAA results was obtained. Compared with the bulk results, a very important enrichment of Ag together with a decrease in Cu can be observed; this effect is especially important for the Ag-rich coins.

Next to the Ag-enriched sub-surface layer, on top of the upper surface of silver coins dark stains, enriched in Cu and other elements such as Fe, S and Cl, can also occur. This may be the result of a heat treatment, causing Cu from within the bulk to rise to the surface, because of oxidation of the silver by atmospheric gases leading to the formation of black $Ag_2S$ or AgCl precipitates or simply as a result of mechanical wear and soiling during the use of the coins.

To illustrate this, Fig. 10 shows elemental maps collected with the polycapillary-based system from a Belgian silver coin of 1901, showing a royal portrait in relief. In the Compton and Rayleigh maps, showing the variation

**Figure 8.** Photograph of a Japanese 18th century vase.

Copyright © 2000 John Wiley & Sons, Ltd. 

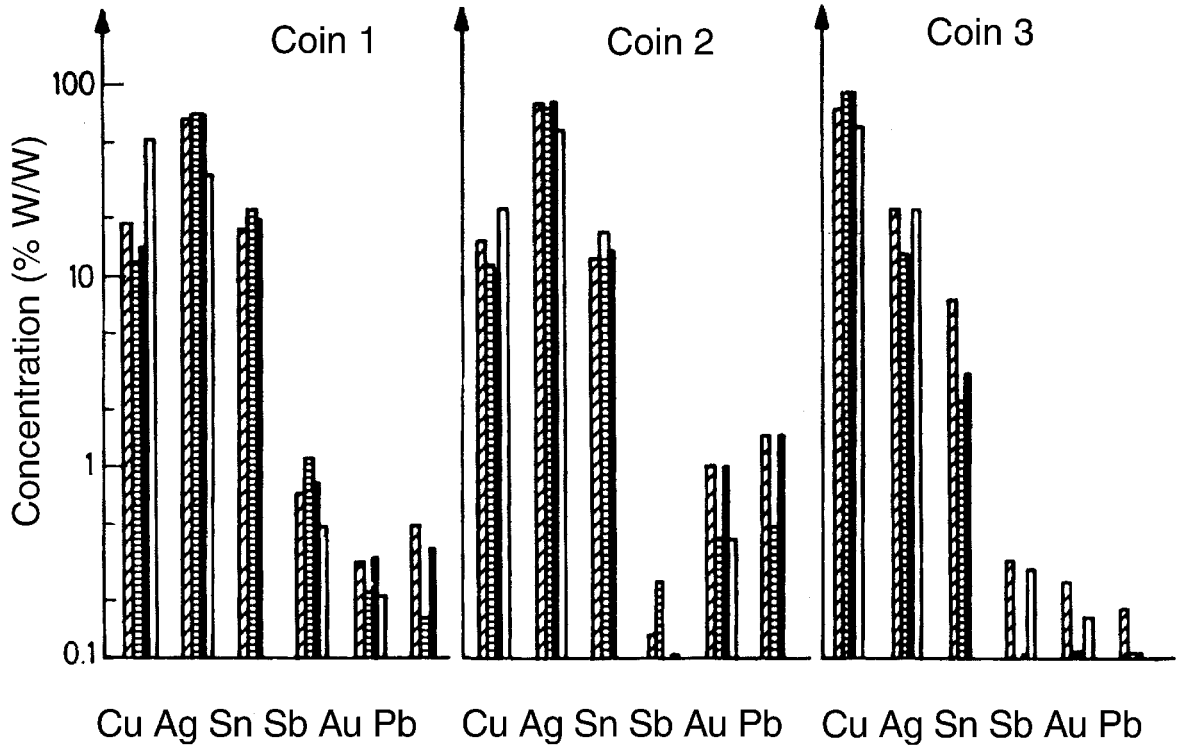


**Figure 9.** Quantitative data obtained from three Gallic coins by means of (a) SR-XRF at 17 keV primary energy (hatched bar), (b) at 35 keV (striped bar), (c) 2 MeV PIXE (full bar) and (d) neutron activation analysis (empty bar).

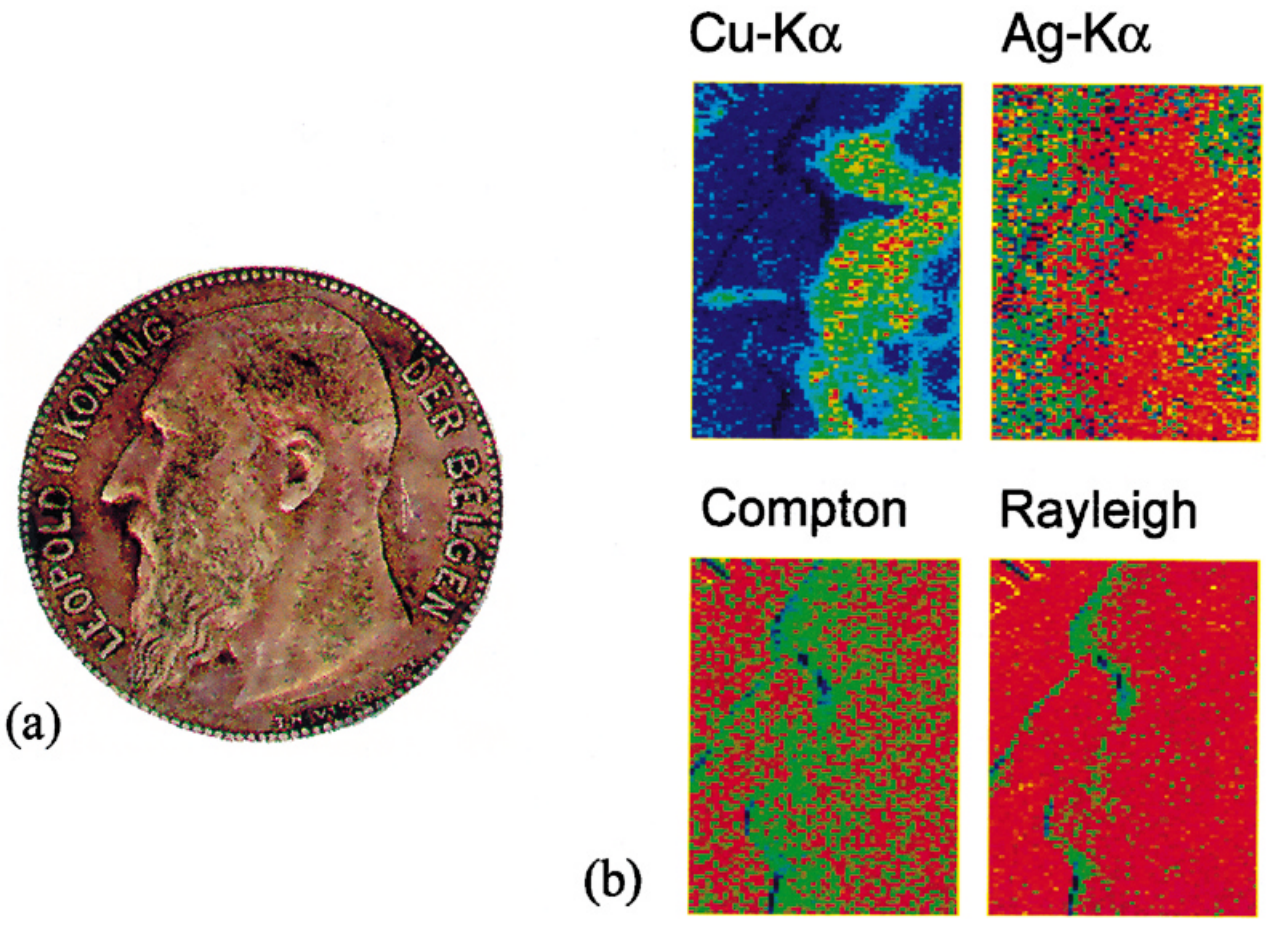


**Figure 10.** Optical photograph (left) and x-ray maps (right) of Cu, Ag and the scatter peak intensities obtained from a 19th century Belgian silver coin. The scanned area is 10 × 5 mm. The maps labelled 'Compton' and 'Rayleigh' show the variation of the scatter peak intensities throughout the scanned area, highlighting the surface topology. Low intensity values are denoted by blue colours, medium intensities by green and high intensities by red.

Copyright © 2000 John Wiley & Sons, Ltd. 

of the scatter peak intensity throughout the scanned area, the surface topology is clearly visible. At strongly curved areas of the coin surface (facial features of portrait), where the take-off angle of the radiation towards the detector is smaller than 45°, the absorption path of the scattered radiation inside the metal is longer. Accordingly, these areas have a lower intensity in the scatter intensity maps. In the Cu maps, an area showing a much higher Cu signal can be seen; this area corresponds to a blackish stain on the coin surface. In none of the different areas on the coin however, was the correct Cu/Ag ratios found: inside the stain, the ratio is overestimated (too much Cu), while outside it, an excess of Ag is observed, even when the more penetrant Ag K radiation is used to determine the Ag content. This necessitates the removal of some of the upper surface layers to allow analysis of the underlying alloy.

Recently, the authors have evaluated a micro-polishing method in combination with $\mu$-XRF analysis of the exposed sub-millimetre sized surface for accurate determination of the silver content in ancient Ag–Cu coins.[46] The procedure involves the use of a rotating stainless-steel grinding tool of sub-millimetre cross-section to remove the upper, Ag-enriched surface layer in a very small area of the coin. The grinding step, which produces an unenriched but fairly rough surface [see Fig. 11(a)], is followed by a micro-polishing step. By applying diamond paste (30–10 μm grain size) on the exposed area by means of a rotating wooden rod, a smoothly polished area is obtained [see Fig. 11(b)]. The polishing step was found to be required in order to improve the reproducibility of the analysis. A systematic study using the polycapillary instrument revealed that this procedure allows one to determine the Ag content in corroded coins with an accuracy of better than 1% provided that the measurements are performed in the centre of the circular depression shown in Fig. 11(b).

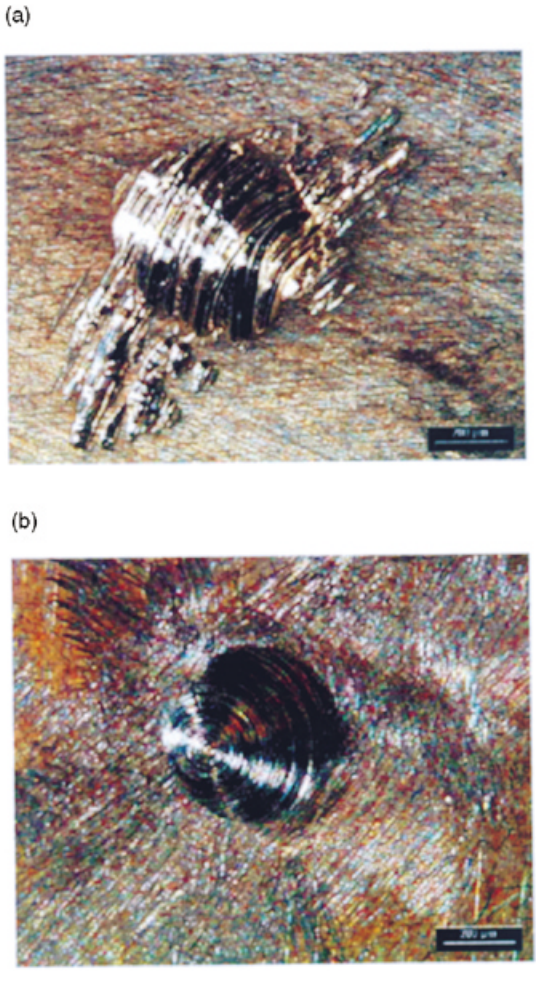


**Figure 11.** Electron micrographs obtained after (a) micro-grinding and (b) micro-grinding and micro-polishing of the surface of an Ag–Cu alloy coin.

In the 19th century, great interest arose in the ancient Egyptian civilization; many museums in the world currently own a collection of small Egyptian statues of a religious nature in stone or bronze.[47] To a varying extent, most metal statues have developed a corrosion layer that prevents reliable analysis of the Cu-based alloys from which the objects were made.[48,49] This alteration layer is much thicker (several tens to several hundreds of micrometres) than in the case of silver alloys. Nevertheless, information on the original copper alloy is of interest since it can be used to trace the evolution of Egyptian metallurgy in the period from 3000 BC to the first century.[50,51] Analyses of this type can also be used to distinguish between original pieces and contemporary or earlier forgeries[3] or to establish, for example, whether all parts of a statue are made from the same alloy. By employing micro- or milli-beam XRF, several parts of a statue can be examined under reproducible conditions (e.g. by avoiding strongly curved surfaces), whereas for quantitative analysis of the underlying metal, areas of the statue which are corrosion free can be used. If these are not available, only small areas of the corrosion layer (e.g. on the base of a statue) need to be removed, as explained above.

As an example, Table 2 lists quantitative analysis results obtained from a statue of the god Nefer-hotep represented in Fig. 12 (about 40 cm high, from the collection of the Museum Vleeshuis, Antwerp, Belgium[47]) of exceptional quality, dated to the XXII–XXIII dynasty (ca 1000 BC).[52] It was analysed non-destructively by means of a simple milli-XRF set-up consisting of a collimated low-power mini-focus tube (70 W, 250 μm focal spot on Mo anode), yielding a pencil beam of ca 300 μm diameter and a 30 $mm^2$ Si(Li) detector. A fundamental parameter method was used to obtain quantitative results. Analysis of brass and bronze standards revealed that Cu, Zn, Sn and Pb (the elements most informative on Cu metallurgy in this period) could be determined with a relative accuracy of ca 10% down to the 100 ppm level. The body of the statue is copper coloured, has a very smooth surface and shows only a very thin corrosion layer. The double crown and base of the statue are darker in colour and have a rougher texture, suggesting the presence of a thicker corrosion crust and possibly the use of a different alloy composition. Both crown and base were made separately from the body. Since the data in Table 2 suggest a difference in composition between the body of the statue (legs, front of body) and its crown and base, on the bottom side of the base, a few square millimetres of the corrosion layer were polished away, exposing the original metal. The results obtained after polishing are also shown in Table 2 and indicate that there is in fact no large difference in composition between base and body and that probably all parts of the statue were made using a similar alloy composition and in the same

Copyright © 2000 John Wiley & Sons, Ltd. 

**Table 2. Quantitative results (concentration, % w/w) local analysis of different locations on the statue shown in Fig. 12**

| | Body | | | | | Base (unpolished) | | | Base (polished) | | |
|---|---|---|---|---|---|---|---|---|---|---|---|
| | | | | Crown | | | | | | | |
| Element | Right leg | Front | Head band | Lower | Upper | Front | Back | Bottom A | Bottom A | Bottom B | Bottom C |
| Fe | 0.12 | 0.14 | 0.25 | 0.09 | 0.09 | 0.11 | 0.11 | 0.15 | 0.09 | 0.07 | 0.08 |
| Cu | 81.2 | 82 | 76.5 | 72.8 | 75.8 | 72.6 | 70.7 | 71.4 | 80 | 84.9 | 84.8 |
| Ag | 0.05 | 0.04 | 0.12 | 0.18 | 0.13 | 0.17 | 0.19 | 0.13 | 0.07 | 0.06 | 0.06 |
| Sn | 13.7 | 12.9 | 14.8 | 19.8 | 17.5 | 22.3 | 21.6 | 21 | 15.3 | 12.2 | 12.2 |
| Pb | 4.8 | 4.5 | 7.6 | 6.5 | 6.2 | 4.3 | 7 | 6.7 | 4.6 | 2.5 | 2.5 |

**Figure 12.** Photograph of a statue of the god Nefer-hotep (Museum Vleeshuis, Antwerp, Belgium) dated to the XXII or XXIIIth dynasty. The height of the statue is ca 25 cm.

workshop. Patinas of bronze objects of this kind generally are found to contain less Cu and more Pb and Sn than the original alloy.[53] The compositions found after polishing are consistent with literature data on this type of material and period.

It is clear that the possibilities for non-destructive analysis of $\mu$-XRF can contribute significantly to a better understanding of ancient metallurgical techniques while requiring minimal interventions on the objects themselves.

In the period 1824–1828, Russia issued about 15 tons of platinum coins of 3, 6 and 12 roubles in an attempt to employ its Uralian ore resources. These coins are considered to be numismatic peculiarities and have therefore become collectors' items. After their withdrawal, additional mintings took place (called 'Novodel' mintings) until 1890, and during a long period after that a considerable number of falsifications were also made. To make the original coins, the natural Pt alloys containing ca 75% (w/w) Pt had to be refined to obtain a technically pure platinum powder for forging and minting. The Pt powder also contained irregularities of various nature such as gold- and copper-rich inclusions. Auer *et al.*[54] used several analytical techniques such as electron probe x-ray microanalysis, $\mu$-XRF, conventional WD-XRF and XRD for analysing seven of these coins. Six of the coins were found to contain considerable quantities of elements other than Pt, mostly Fe, Ir and Ni. Only one coin, dated to 1828, was found to consist of technically pure Pt. This coin originated from a Novodel minting and was probably struck at the end of the 19th century. The laboratory-built micro-XRF facility at the Institut für Spectrometrie und Angewandte Spectroskopie (ISAS, Dortmund, Germany) was used to analyse the gold inclusions in a coin minted in 1838. These inclusions are indicators of some form of 'mechanical dilution' of the refined platinum with natural Pt alloys prior to its minting, probably indicating fraudulent practices.

## Beyond compositional microanalysis

**Glass corrosion.** In Fig. 13(a), a backscattered electron micrograph and x-ray maps are shown of a cross-sectioned fragment of one of the Roman glass fragments from the Qumrân site (see above). It was buried in moist Jordanian soil for about 1900 years.[22,55] As a result of the interaction with ground water during this period, a leached or corroded layer was produced, in which a number of the original cations of the glass (mainly $Na^+$, $K^+$ and $Ca^{2+}$) were replaced by protons and other dissolved cations from the groundwater. Owing to a number of other physical and chemical processes that have occurred inside the leached layer and in the surface crust on top of the original surface, a chemically and physically complex multilayered structure was formed. For example, in Fig. 13(a) a parallel corrosion front next to a hemispherical corrosion body can be distinguished.

In order to obtain a better understanding of the mechanisms that led to the formation of these complex structures, the distribution and migratory patterns of various (trace) elements (e.g. Mn, Bi, Sr and Zr) should be determined and correlated with their ionic size and nature of their bonding to the glass network structure in the various layers.[29] A comparison of elemental maps generated by $\mu$-XRF and $\mu$-PIXE[9] indicated that both techniques provide approximately equivalent information on the distribution

Copyright © 2000 John Wiley & Sons, Ltd.

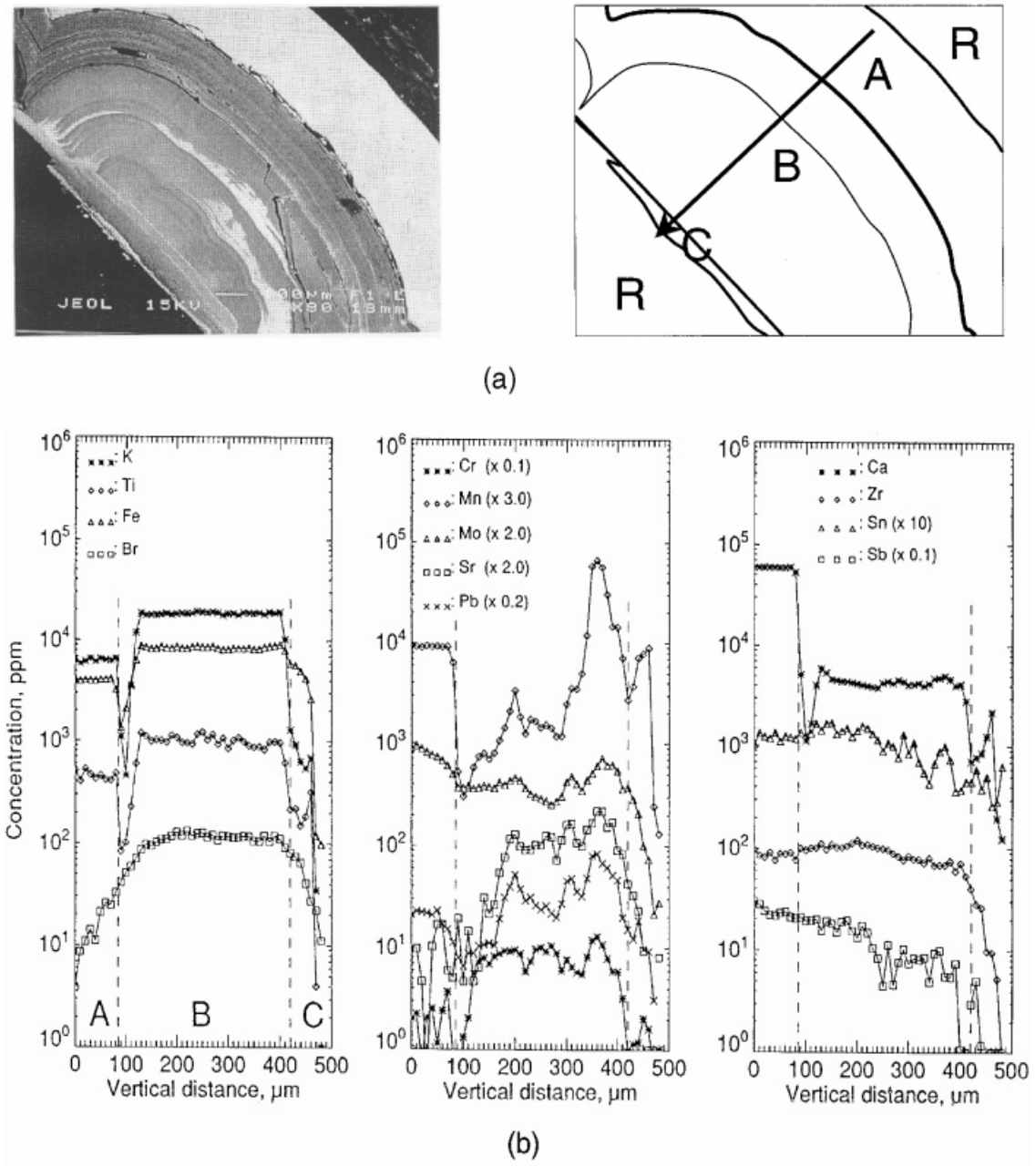


**Figure 13.** (a) Backscattered electron micrograph of a corroded glass sample (cross-sectional view). The object was excavated at Khirbet Qumrân, Israel. R, embedding resin; A, original glass; B, corroded layers, C, precipitation crust. The arrow indicates the location of the line scan shown in (b). (b) Quantitative line profiles across the corrosion layer of a corroded Roman glass sample. A, original glass; B, corrosion layer; C, precipitation crust on top of glass surface.

of trace constituents such as Cr, Ni, Cu, Zn, Pb, Bi, Sr and Mo. In Fig. 13(b), the quantitative line profiles are shown for a number of major, minor and trace elements across the corrosion layer, as obtained by $\mu$-SRXRF.

Most trace elements are enriched in the corrosion layer, with the exception of Sn, Sb and Zr that remain at the same level as in the bulk glass. For the tetravalent elements Sn and Zr this is not surprising since they take part in the formation of the glass network; Sb behaves similarly to Sn, although some leaching is observed. Some of the elements are enriched (K, Fe, Ti, Br) and show a uniform distribution throughout the alteration layer. Others elements, however, such as Cu and Bi [not shown in Fig. 13(b)], are concentrated on the boundary layer between the original glass and corrosion or show an asymmetric distribution and are enriched in the Mn-rich precipitation areas [the bright areas in Fig. 13(a)].

These data, together with those obtained from other corroded glass samples, show that the corroded layer is not formed as the result of a simple, monotonous leaching process during which the original major cations of the glass ($Na^+$, $Ca^{2+}$) are replaced by others ($K^+$, $Mg^{2+}$). Rather, a complex cycle of leaching followed by physical separation of the leached layer from the substrate glass, followed by renewed leaching, etc., must have taken place. In the cavities between the different parts of the cracked-off layers, Mn can precipitate (presumably in the $MnO_2$ state), causing also other trace elements (present in the ground water) to become enriched in these areas.

Copyright © 2000 John Wiley & Sons, Ltd.

Figure 13(c) shows the distribution of different elements throughout the corrosion body. However, in order to obtain a better understanding of the (various phases of) the corrosion process, this information should be complemented by chemical information, i.e. localized information on the presence of certain elements in a particular chemical state. In the case of the corroded glass, knowledge on the distribution of various Mn species [such as Mn in the 2+ (MnO), 3+ ($Mn_2O_3$) or 4+ ($MnO_2$) state] can contribute significantly to insight into the corrosion mechanism. Such information may be obtained by taking advantage of the fact that the K-adsorption edge of Mn shifts over several eV towards higher energies with increasing oxidation state. When Mn K$\alpha$ fluorescence is induced on the micro-scale by means of a focused, monochromatic beam of which the energy can be changed within a certain range around the Mn K-edge position, while keeping the same position of the microbeam on the sample, localized XANES (x-ray absorption near edge structure) measurements can be performed. In Fig. 14, x-ray maps obtained by scanning a small (300 × 300 μm) area on the sample in Fig. 13(a) are shown. A monochromatic beam of ca 3 × 5 μm cross-section was employed. The measurements were performed at the ID22 Beamline of ESRF. The scanning range included an area which features a strong contract in the backscattered electron image of Fig. 13(a) and which also shows localized enrichment of Mn. The Si, Cl, K, Ca, Ti and one of the Mn images [Mn (b)] were obtained by using a primary energy of 6.550 keV; at this energy, Mn in the 2+ state is efficiently excited (and will therefore produce Mn K fluorescent radiation) whereas Mn in the 4+ state is not. The other Mn image [Mn (a)] was obtained by repeating the scan at slightly higher energy (6.564 keV) so that also $MnO_2$ (and other Mn species in the 4+ form) can contribute to the detected Mn K radiation. At first sight, both Mn images indicate that in the scanning area, Mn enrichment has taken place and that the spatial distribution of the Mn throughout the corrosion layer is not well defined. However, when (after appropriate scaling) both Mn K intensity images are subtracted from each other [Mn (a) − $x$Mn (b)], an image with much better contrast is obtained. The difference image corresponds to the contribution from $Mn^{4+}$ (likely to be present as $MnO_2$) and therefore represents a *chemical* $Mn^{4+}$ rather than an *elemental* Mn map. The scaling factor $x$ was adjusted in such a way that the peripheral areas of the difference map completely cancelled out. The difference image clearly indicates that inside the successive layers itself of the corrosion body, no $MnO_2$ crystal formation has taken place; $MnO_2$ is exclusively confined to cavities between successive layers. This is an important conclusion since it may help direct the development of appropriate restoration treatments of corroded glass (e.g. by the introduction of Mn-reducing fluids into the cavities); also, during evaluation and intercomparison of alternative treatments, the effectiveness of the chemical transformations may be monitored in detail without dissolution of the material itself.

**Combined $\mu$-XRF and $\mu$-XRD analysis of inclusions in iron artifacts.** Dillman *et al.*[56] studied inclusions in ferrous archaeological artifacts by using a combination of micro-diffraction and micro-fluorescence at the LURE $\mu$-XRF station. For this purpose, a Bragg–Fresnel multilayer lens (BFML) was used to focus synchrotron radiation into a spot of a few square micrometres. Sixteen ferrous objects were studied, originating from the 1st, 5th and 17–19th centuries. Seven of the objects were manufactured using the 'direct process' to obtain iron from iron ore;[57] the iron of the other nine objects was obtained by the 'indirect'

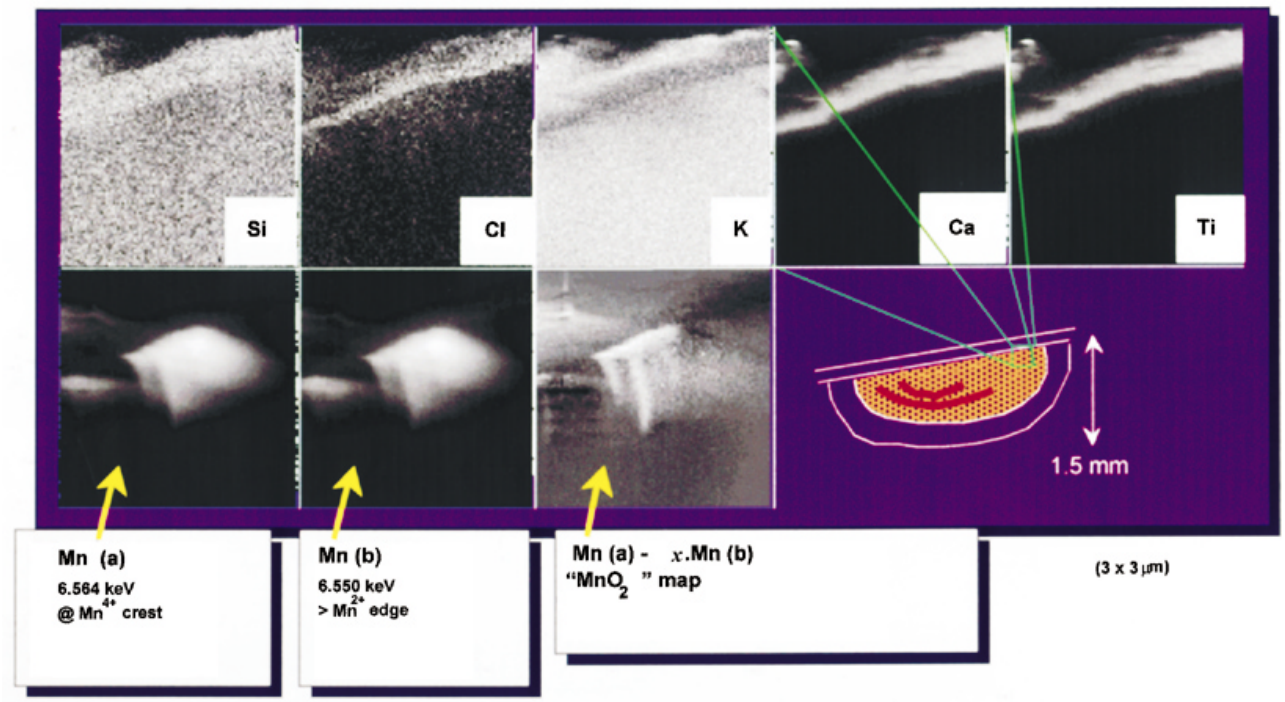


**Figure 14.** Elemental maps of various elements obtained from a 300 × 300 μm area on the sample shown in Fig. 13. A monochromatic beam of ca 3 × 5 μm cross-section was employed with tunable energy at the ESRF ID22 Beamline. The difference between the two Mn images results in an 'oxidation state'-specific map of $Mn^{4+}$, present as $MnO_2$ precipitates in the cavities between the successive layers forming the corrosion body.

Copyright © 2000 John Wiley & Sons, Ltd. 

process. One of the investigated objects was a girder from the Eiffel Tower in Paris.

The direct process of iron reduction was employed in low shaft furnaces in which the melting temperature of the iron is not reached. The resulting iron or steel contains many non-metallic inclusions; from the 10th century onwards, the 'indirect process' was developed, in which the iron ore is heated to a much higher temperature so that iron reduction takes place in the liquid phase; this also introduces carbon into the iron. In a second stage, the resulting cast iron (an alloy of Fe, Si and C) can be refined by oxidation of the carbon.

The study of the inclusions trapped in the iron matrix allows the identification of the type of reduction process employed and complements historic and iconographic data on the evolution of these techniques.[58]

For the $\mu$-XRF and $\mu$-XRD measurements, the inclusions were separated from the iron matrix in a multi-step process.[56] In Table 3, an overview is presented of the mineral phases that were identified in the inclusions of each artifact; some of the inclusions were as small as 20 μm in diameter.

In the materials obtained via the direct process, in all cases, aluminium-containing phases such as $(Mg,Al)Fe_2O_4$, hyrcinite or galaxite are encountered in the inclusions. Fayalite ($Fe_2SiO_4$) and wustite were also found. The latter minerals were also detected in the inclusions of the materials obtained by means of the indirect process.

Dillman *et al.*[56] suggested that the presence of the Al minerals may be used to discriminate between the direct and the indirect processes. When the direct process is employed, Al can enter into the iron from the ore (up to a few percent only) or from the clay lining of the furnace. On the other hand, Al is known to be lower in concentration in cast iron which is obtained by means of the 'indirect' process.

## Towards *in situ* $\mu$-XRF investigations

Conventionally, ED-XRF is performed on relatively small-scale but still stationary instruments. In direct excitation instruments, the major reason for the size and stationary nature of the instrument is the presence of a bulky Dewar vessel for cryogenic cooling of the solid-state detector. In the last 5 years, various efforts have been made to develop non-liquid nitrogen equivalents of the Si(Li) detector; a comprehensive review of these developments was given by Ellis *et al.*[59] Some of these devices are being used in commercially available or laboratory-built compact XRF devices which may be used for on-site investigations of archaeological and/or artistic materials.[60] Specific examples are the $HgI_2$ detector which is incorporated into a radioisotope-based portable XRF instrument (TN9000, Thermo Unicam, Cambridge, UK)[61,62] and an Si-PIN detector (Amptek, Bedford, MA, USA).[63] With some of the devices, small beams (of ca 1 $mm^2$ cross-section) may also be generated for local analysis.

**Secondary target instruments.** Cesareo *et al.*[64] described the use of different source–detector combinations for performing *in situ* analyses of works of art and illustrated the capabilities of these instruments with analysis results derived from bronze and gold objects, ceramics, faience

**Table 3. Identified phases in inclusions of ferrous artifacts**

| Artifact | Date | Type | Phases identified: Fayalite | Wustite | Magnetite | Others |
|---|---|---|---|---|---|---|
| Iron ingot 1 | 1939 | Indirect | | x | x | Mn-fayalite |
| Screw | 1878 | Indirect | x | x | | $Fe_9O_8PO_4$ |
| Nut | 1878 | Indirect | x | | | $Fe_9O_8PO_4$ |
| Girder 1 | 1878 | Indirect | | | | Troilite FeS |
| Girder 2 | 1888 | Indirect | x | x | x | Hematite, $Fe_9O_8PO_4$ |
| Mining tool 1 | 19th C. | Indirect | x | x | | |
| Mining tool 2 | 18th C. | Indirect | x | x | x | |
| Mining tool 3 | 17th C. | Indirect | x | x | x | Goethite,[b] quartz |
| Iron rod | 17th C. | Indirect | x | x | x | Troilite |
| Iron ingot 2 | 5th C. | Direct | x | x | x | $(Mg,Al)Fe_2O_4$ |
| Iron ingot 3 | 5th C. | Direct | x | x | x | Hercynite, $(Mg,Al)Fe_2O_4$ |
| Iron ingot 4 | 1st C. | Direct | x | x | x | |
| Iron chunk | 1st C. | Direct | x | x | x | Galaxite |
| Iron ingot 5 | 1995 | Direct[a] | x | x | x | Alumine, hercynite, quartz, hematite |
| Iron bloom 1 | 1995 | Direct[a] | x | x | x | Alumine, hercynite, $(Mg,Al)Fe_2O_4$ |
| Iron bloom 2 | 1995 | Direct[a] | x | x | | Galaxite, hematite, $(Mg,Al)Fe_2O_4$ |

[a] Modern laboratory reconstruction.
[b] Present due to internal corrosion.

Copyright © 2000 John Wiley & Sons, Ltd.

and porcelains and pigmented materials on illuminated manuscripts. Measurements were performed in the Museo di Villa Guilia (Rome, Italy), the Museo Sanna (Sassari, Italy), the Museo de Antropologia and the Museo del Templo Major (Mexico City, Mexico) and the Museo de la Ciudad (Havana, Cuba). Most of the instruments consisted of a W-anode x-ray tube (Radiolight, 20–80 kV, 5 mA), equipped with Ba or Mo secondary targets and either a liquid nitrogen-cooled Si(Li) or HPGe detector or a compact Peltier-cooled Si-PIN or $HgI_2$ detector. The authors claimed that since the heaviest element of interest in archaeometric investigations is Ba (Ba K$\alpha$ at 32 keV), the reduced quantum efficiency of the Si-PIN (of only 300 μm thickness) does not present serious limitations. An energy resolution for the latter two detectors of 280 and 200 eV, respectively, was reported. They also described the use of a collimated direct excitation set-up, consisting of a low-power tube operated typically at 35 kV and 0.3–0.5 mA of which the outgoing radiation is collimated by a 2.5 mm diameter aperture. The use of this type of device, sometimes in combination with near-infrared reflectometry for non-destructive pigment identification in frescoes from the Roman and Renaissance period (including Michelangelo's *Last Judgement* in the Sistine Chapel, Rome) has been described by various authors.[65–67]

Lu *et al*.[68] constructed a small-beam XRF spectrometer for the assay of precious metals in jewellery that utilizes a 0.5–1 $mm^2$ collimated beam from a low-power x-ray tube coupled to a high efficiency proportional counter detector.

**Use of compact focusing optics.** One step towards the realization of the use of small (i.e. sub-millimetre) beams in compact, low-power set-ups is to use equally compact x-ray lenses. With 50 W tubes and apertures, the primary beam needs to have a cross-section of at least 300–500 μm to allow for measurements within reasonable counting times (500–1000 s per point). The fact that some polycapillaries only produce beams of 50–100 μm diameter does not present a limitation in investigations where mostly sub-millimetre sized (or larger) features of macroscopic objects are analysed. The marked advantage of polycapillary lenses over monocapillary concentrators resides with the fact that they form a focal spot at a considerable distance (several centimetres) from the end of the lens whereas with monocapillaries the smallest beam diameters are reached at the point where the beam leaves the capillary. This allows for a completely non-contact, non-destructive kind of investigation and makes polycapillary lenses ideal for local analysis of sensitive, precious and/or unique objects of macroscopic size such as statues, miniature paintings, coins, utilitarian objects in glass or metal (goblets, vases, etc.) and the (often multi-coloured) decorations which are applied to them. Vekemans *et al*.[69] described the use of such devices for the local analysis of enamel paints on Chinese porcelain and for the quantitative analysis of genuine and counterfeit Indian brass statues from the 16th century. By using the lenses instead of an equivalent collimator, an increase in intensity by a factor 7–20 was obtained. For the measurements, an Mo rotating anode, operated at relatively low power (10 mA, 50 kV) was employed. These results indicate that in combination with a 50 W mini-focus tube (where these lenses can capture a much larger fraction of the total flux that exits from the tube) sub-millimetre beams of high intensity can be readily obtained. Carpenter and co-workers.[70] reported a factor of 44 intensity gain when a monolithic polycapillary device was used to optimize the $\mu$-XRF instrument at the Oak Ridge Center for Manufacturing Technology.

## CONCLUSIONS

In this paper, the current possibilities and future potential of $\mu$-XRF for the analysis and characterization of archaeological artifacts and objects of art have been discussed and illustrated with a number of selected examples. The applications listed are not intended to be exhaustive; there is a bias in the examples that were selected from the field of experience of the laboratory of the authors.

In general, it is important to point out that the application of analytical methods in the field of archaeology is aimed at answering one or more questions derived from human history or the history of art. Present-day concepts in this particular field are very often based on theories that are lacking any real experimental proof.

As in many other 'problem-solving' areas of research, there exists no unique and fail-safe method that can be applied for tackling such problems. Rather, a plethora of analytical methods should be considered for exploitation, each of which has its own specific advantages and limitations for the problem at hand. In particular, all these methods take into account the specific drawbacks involved in sampling and analysis of archaeological samples. The most important drawback in this area of analysis is that very often the samples are unique or too valuable to be destroyed or altered by sampling. This is a major reason for the predilection for microanalytical methods in this area. The other and more fundamental reason for the emphasis on microanalysis is that very often the sample which needs to be selected for analysis is microscopically small, or the problem that needs to be addressed concerns a microscopic or extremely small volume.

In this respect, $\mu$-XRF offers a unique set of characteristics for solving many of the problems that arise. The method is completely non-destructive, can be applied to minute sample amounts, sensitive, versatile and applicable to many materials.[2]

## REFERENCES

1. P. T. Craddock and N. D. Meeks, *Archaeometry* **29**, 187 (1987).
2. Ch. Lahanier, G. Amsel, Ch. Heitz, M. Menu and H. H. Andersen, *Nucl. Instrum. Methods Phys. Res. B* **14**, 1 (1986).
3. F. Adams, A. Adriaens, A. Aerts, I. De Raedt, K. Janssens and O. Schalm, *J. Anal. At. Spectrom.* **12**, 257 (1997).
4. K. G. Malmqvist, in *Particle Induced X-Ray Emission Spectrometry (PIXE)*, edited by S. A. Johansson, J. L. Campbell and K. G. Malmqvist, Chapt. 7. Wiley, Chichester (1995).

Copyright © 2000 John Wiley & Sons, Ltd. 

5. S. A. Johansson and J. L. Campbell, *PIXE: A Novel Technique for Elemental Analysis*. Wiley, Chichester (1988).
6. A. M. Pollard and C. Heron, *Archaeological Chemistry*. Royal Society of Chemistry, Cambridge (1996).
7. F. Adams, K. Janssens and A. Snigirev, *J. Anal. At. Spectrom.* **13**, 319 (1998).
8. M. Milazo and C. Cicardi, *X-Ray Spectrom.* **26**, 211 (1997).
9. K. Janssens, B. Vekemans, L. Vincze, F. Adams and A. Rindby, *Spectrochim. Acta, Part B* **51**, 1161 (1996).
10. K. Janssens, L. Vincze, B. Vekemans, F. Adams, M. Haller and A. Knöchel, *J. Anal. At. Spectrom.* **13**, 339 (1998).
11. L. Vincze, K. Janssens, F. Adams and K. W. Jones, *Spectrochim. Acta, Part B* **50**, 1481–1500 (1995).
12. L. Vincze, K. Janssens, B. Vekemans and F. Adams, *J. Anal. At. Spectrom.* **14**, 529–533 (1999).
13. K. Janssens, L. Vincze, A. Aerts, F. Adams and J. Hertogen, *X-Ray Spectrom.* **26**, 333 (1997).
14. A. Knöchel and M. Haller, *J. Trace Microprobe Tech.* **14**, 461 (1996).
15. K. Janssens, L. Vincze, B. Vekemans, C. T. Williams, M. Radtke, M. Haller and A. Knöchel, *Fresenius' J. Anal. Chem.* **363**, 413–420 (1998).
16. L. Vincze, K. Janssens, B. Vekemans and F. Adams, *Spectrochim. Acta B* **54**, 1711 (1999).
17. B. Lai, B. Yun, D. Legnini, Y. Xiao, J. Chrzas, P. J. Vicaro, V. White, S. Bajikar, D. Denton, F. Cerrina, E. Di Fabrizio, M. Gentili, L. Grella and M. Baciocchi, *Appl. Phys. Lett.* **61**, 1877–1879 (1992).
18. N. Gao and D. Gibson, *X-Ray Spectrom.* **28**, 75 (1999).
19. E. V. Sayre and R. W. Smith, *Science* **133**, 1824 (1961).
20. K. Janssens, I. Deraedt, O. Schalm and J. Veeckman, *Microchim. Acta. Suppl.* **15**, 253 (1998).
21. B. Velde and G. Sennequier, *Annales du 9 Congrés de l'Association pour l'Histoire du Verre*, 127–147 (1985).
22. R. Donceel and P. Donceel-Voûte, *Ann. N. Y. Acad. Sci.* **772**, 1 (1994).
23. A. Aerts, K. Janssens, F. Adams and L. Wouters, *J. Arch. Sci.* **26**, 883 (1999).
24. P. Donceel-Voûte, *Archeologia* **298**, 24 (1994).
25. B. Velde and C. Gedron, *Archaeometry* **22**, 182 (1980).
26. B. Velde, *Oxford J. Archaeol.* **9**, 105 (1990).
27. P. Hoffmann, *Fresenius. J. Anal. Chem.* **349**, 320 (1994).
28. A. Aerts, PhD Thesis, University of Antwerp, (1998).
29. R. G. Newton, *Glass Technol.* **21**, 173 (1980).
30. E. V. Sayre, in *Advances in Glass Technology*, edited by F. R. Matson and G. E. Rindone, Vol. 2, p. 263–282. Plenum Press, New York (1963).
31. B. Velde and A. Hochuli, *Annales du 13 Congrès de l'Association International pour l'Histoire du Verre*, 185–192 (1995).
32. K. Janssens, I. Deraedt, O. Schalm and J. Veeckman, *Microchim. Acta, Suppl.* **15**, 253 (1998).
33. K. H. Wedepohl, *Die Herstellung Mittelalterlicher und Antiken Gläser*. Steiner, Stuttgart (1993).
34. M. Verità and T. Tonianto, *Riv. Staz. Sperimentale Vetro (Murano)* **20**, 169 (1990).
35. M. O. Figueiredo, J. P. Veiga and T. Pereira da Silva, *Proceedings of the 6th International Conference on 'Non-destructive Testing and Microanalysis for the Diagnostics and Conservation of the Cultural and Environmental Heritage,' Rome, May 17–20, 1999*, pp. 1769–1779 (1999).
36. A. Knöchel and M. Haller, *J. Trace Microprobe Tech.* **14**, 461 (1996).
37. H. Mommsen, Th. Beier, H. Dittmann, D. Heimermann, A. Hein, A. Rosenberg, M. Boghardt, E.-M. Manebutt-Benz and H. Halbey, *Archeometry* **38**, 347 (1996).
38. T. Cahill, B. Kusko and R. N. Schwab, *Nucl. Instrum. Methods. Phys. Res. B* **181**, 205 (1981).
39. T. Cahill, B. Kusko, R. A. Eldred and R. N. Schwab, *Archaeometry* **26**, 3 (1984).
40. R. N. Schwab, *Library Trends* **36**, 53 (1987).
41. R. N. Schwab, T. A. Cahill, B. H. Kusko, R. A. Eldred, G. Moller and D. Dutschke, *Pap. Bibliogr. Soci. Am.* **8**, 305 (1986).
42. C. H. Bloy, *A History of Printing Ink, Balls and Rollers 1440–1850*. Buttersworth, London (1967).
43. S. Larsson, Thesis, Department of Physics, Chalmers University of Technology, Goteborg. Bibliotekets ReproService, Goteborg (1991).
44. B. Stocklassa, G. Nillson, N. Paulson, paper presented at the European Conference on EDXRS, Myconos, Greece, May 30–June 6, (1992).
45. I. Brissaud, J. X. Wang and P. Chevallier, *J. Radioanal. Nucl. Chem.* **131**, 399 (1989).
46. I. Deryck and K. Janssens, *Spectrochim. Acta*, submitted for publication.
47. A. Oost (ed), *Egypte Onomwonden*. Catalogue of Egyptian Artefacts of the Museum 'Vleeshuis', Antwerp (1995); (in Dutch).
48. L. Robbiola, I. Queixalos, L. P. Hurtel, M. Pernot and C. Volfovsky, *Stud. Conserv.* **33**, 205 (1988).
49. L. Robbiola and C. Fiaud, *Ed. Rev. Métall.* **6**, 156 (1993).
50. M. Wuttmann, in *Proceedings of the First International Conference on Ancient Egyptian Mining and Metallurgy and Conservation of Metallic Artefacts*, FIFAO, Cairo (1996).
51. M. Wuttmann, in *Balat I, Le Mastaba de Medoe-Nefer, Annexe III: Analyse et Étude du Métal Cuivreux de Certains Objets*, edited by M. Valloggia, 215–220. FIFAO 31/1, Cairo (1986).
52. G. Vittiglio, K. Janssens, B. Vekemans, F. Adams and A. Oost, *Spectrochim. Acta, Part B* **54**, 1697 (1999).
53. J. Tate, *Nucl. Instrum. Methods. Phys. Res. B* **14**, 20 (1986).
54. E. Auer, Th. Rehren, A. von Bohlen, D. Kirchner and R. Klockenkamper, *Metalla (Bochum)* **5**, 71 (1998).
55. K. Janssens, A. Aerts, L. Vincze, F. Adams, C. Yang, R. Utui, K. Malmqvist, K. W. Jones, M. Radkte, S. Garbe, F. Lechtenberg, A. Knöchel and H. Wouters, *Nucl. Instr. Methods Phys. Res. B* **109/110**, 690 (1996).
56. P. Dillman, P. Populus, P. Chevallier, P. Fluzin, G. Beranger and A. Firsov, *J. Trace Microprobe Tech.* **15**, 251 (1997).
57. G. Magnusson (ed). *The Importance of Iron Making, Technical Innovation and Social Change, Parts I and II. Proceedings of the Norberg Conference, May 8–13, 1995*. Jernkontorest Bergshistoriska Utskott, Stockholm (1995).
58. D. Starley, in *The Importance of Iron Making, Technical Innovation and Social Change, Parts I and II. Proceedings of the Norberg Conference, May 8–13, 1995*, edited by G. Magnussen. Jernkontorest Bergshistoriska Utskott, Stockholm (1995).
59. A. T. Ellis, P. J. Potts, M. Holmes, G. J. Oliver, C. Streli and P. Wobrauschek, *J. Anal. At. Spectrom.* **12**, 461R (1997).
60. R. Cesareo, G. E. Gigante, I. S. Iwanczyk and A. Dabrowski, *Nucl. Instrum. Methods. Phys. Res. A* **380**, 440 (1996).
61. P. J. Potts, P. C. Webb, O. Williams-Thorpe and R. Kilworth, *Analyst* **120**, 1273 (1995).
62. P. J. Potts, P. C. Webb and O. Williams-Thorpe, *J. Anal. At. Spectrom.* **12**, 769 (1997).
63. A. C. Huber, J. A. Pantazis and V. T. Jordanov, in *Proceedings of International Conference on Application of Accelerators in Research and Industry, Denton TX, 1994*.
64. R. Cesareo, G. E. Gigante, A. Castellano, M. A. Rosales, M. Aliphat, F. De La Fuente, J. J. Meitin, A. Mendoza, J. S. Iwanczyk and J. A. Pantazis, *J. Trace Microprobe. Tech.* **14**, 711 (1996).
65. G. Fronterotta, S. Sciuti and M. Vendittelli, *Proceedings of the 6th International Conference on 'Non-Destructive Testing and Microanalysis for the Diagnostics and Conservation of the Cultural and Environmental Heritage,' Rome, May 17–20, 1999*, pp. 257–270 (1999).
66. S. Sciuti, in *Proceedings of the 6th International Conference on 'Non-Destructive Testing and Microanalysis for the Diagnostics and Conservation of the Cultural and Environmental Heritage,' Rome, May 17–20, 1999*, pp. 401–415, (1999).
67. N. Gabrielli and F. Morresi, in *Proceedings of the 6th International Conference on 'Non-Destructive Testing and Microanalysis for the Diagnostics and Conservation of the Cultural and Environmental Heritage,' Rome, May 17–20, 1999*, pp. 2133–2139, (1999).
68. R. Lu, A. Le, Y. Gu, G. Wu and J. Zhu, *Nucl. Instrum. Methods. Phys. Res. B* **104**, 595 (1995).
69. B. Vekemans, K. Janssens, G. Vittiglio, F. Adams, L. Andong and Y. Yiming, *Adv. X-Ray Anal.* **41**, 278 (1998).
70. N. Gao, I. Ponomarev, Q. F. Xiao, W. M. Gibson and D. A. Carpenter, *Adv. X-Ray Anal.* **39**, 81 (1996).


Copyright © 2000 John Wiley & Sons, Ltd. 